AGU PUBLICATIONS

JGR

Journal of Geophysical Research: Atmospheres

RESEARCH ARTICLE
10.1002/2014JD022259

Key Points:
- Distinct synoptic weather situations result in high precipitation in DML
- High precipitation in ERA-Interim in good agreement with AMPS data
- Meridional moisture flux as a proxy for high precipitation over interior DML

Correspondence to:
C. Welker,
christoph.welker@giub.unibe.ch

Citation:
Welker, C., O. Martius, P. Froidevaux, C. H. Reijmer, and H. Fischer (2014), A climatological analysis of high-precipitation events in Dronning Maud Land, Antarctica, and associated large-scale atmospheric conditions, *J. Geophys. Res. Atmos.*, *119*, doi:10.1002/2014JD022259.

Received 2 JUL 2014
Accepted 4 OCT 2014
Accepted article online 8 OCT 2014

A climatological analysis of high-precipitation events in Dronning Maud Land, Antarctica, and associated large-scale atmospheric conditions

Christoph Welker[1], Olivia Martius[1], Paul Froidevaux[1], Carleen H. Reijmer[2], and Hubertus Fischer[3]

[1]Oeschger Centre for Climate Change Research and Institute of Geography, University of Bern, Bern, Switzerland, [2]Institute for Marine and Atmospheric Research Utrecht, Utrecht University, Utrecht, Netherlands, [3]Oeschger Centre for Climate Change Research and Physics Institute, University of Bern, Bern, Switzerland

Abstract The link between high precipitation in Dronning Maud Land (DML), Antarctica, and the large-scale atmospheric circulation is investigated using ERA-Interim data for 1979–2009. High-precipitation events are analyzed at Halvfarryggen situated in the coastal region of DML and at Kohnen Station located in its interior. This study further includes a comprehensive comparison of high precipitation in ERA-Interim with precipitation data from the Antarctic Mesoscale Prediction System (AMPS) and snow accumulation measurements from automatic weather stations (AWSs), with the limitations of such a comparison being discussed. The ERA-Interim and AMPS precipitation data agree very well. However, the correspondence between high precipitation in ERA-Interim and high snow accumulation at the AWSs is relatively weak. High-precipitation events at both Halvfarryggen and Kohnen are typically associated with amplified upper level waves. This large-scale atmospheric flow pattern is preceded by the downstream development of a Rossby wave train from the eastern South Pacific several days before the precipitation event. At the surface, a cyclone located over the Weddell Sea is the main synoptic ingredient for high precipitation both at Halvfarryggen and at Kohnen. A blocking anticyclone downstream is not a requirement for high precipitation per se, but a larger share of blocking occurrences during the highest-precipitation days in DML suggests that these blocks strengthen the vertically integrated water vapor transport (IVT) into DML. A strong link between high precipitation and the IVT perpendicular to the local orography suggests that IVT could be used as a "proxy" for high precipitation, in particular over DML's interior.

1. Introduction

To study past climatic changes, ice cores have been drilled in the Antarctic ice sheet, which provide information on snow accumulation, temperature as well as the atmospheric concentrations of gaseous and aerosol-bound chemical constituents. To correctly interpret the ice core information, which is derived from the ice phase itself (stable water isotopes, aerosol chemical compounds), a profound understanding of both the glaciological processes that led to ice sheet formation and of the atmospheric conditions under which snow accumulation occurred is indispensable [*Noone et al.*, 1999]. Dronning Maud Land (DML) in the Atlantic sector of East Antarctica has become an area of intensive ice core research in recent years [*EPICA Community Members*, 2006], but also a coastal ice core is supposed to be drilled in this region in the near future. Previous studies showed that in DML, in particular, high-precipitation events can lead to biases in ice cores [*Schlosser et al.*, 2010a].

DML experienced anomalously high snowfall in recent years associated with synoptic weather situations, which enhanced the poleward transport of moisture over DML [*Lenaerts et al.*, 2013]. These high-precipitation events led to considerable regional snow accumulation [*Boening et al.*, 2012].

High-precipitation events strongly influence the surface mass balance of the Antarctic ice sheet, because solid precipitation is the dominant term and largest positive component of the surface mass balance [*King and Turner*, 1997]. Consequently, potential future changes of precipitation and associated snow accumulation over Antarctica could influence global sea level [*Gregory and Huybrechts*, 2006].

DML is characterized by a steep orography (Figure 1) influencing the precipitation climatology. It can be roughly divided into a relatively wet, low-altitude coastal region and a dry, high-altitude interior plateau, separated by mountain and nunatak ranges [*Bromwich*, 1988; *Rotschky et al.*, 2007; *Schlosser et al.*, 2008]. In general, precipitation decreases with increasing distance from the coast and elevation as the air becomes drier and

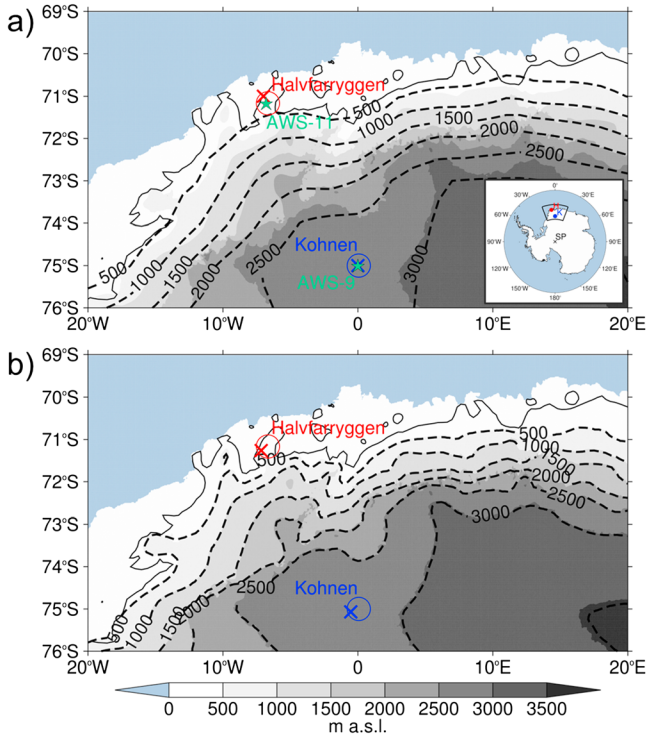

Figure 1. (a) Map of DML showing the locations of Halvfarryggen (red circle) and Kohnen Station (blue circle). The locations of the ERA-Interim grid points closest to Halvfarryggen and Kohnen Station are marked with red and blue cross symbols. Green star symbols indicate the locations of AWS 11 on Halvfarryggen and AWS 9 at Kohnen Station. The filled contours indicate the terrain height in masl according to ETOPO1 1 arc min relief data depicting the top of the Antarctic ice sheet [*Amante and Eakins*, 2009]. The dashed contour lines show the ERA-Interim orography in masl. (b) Analogous to Figure 1a but shown instead of the ERA-Interim orography is the AMPS-WRF orography at 15 km horizontal resolution in masl (dashed contour lines) and the AMPS grid points closest to Halvfarryggen and Kohnen Station (red and blue cross symbols).

colder on its way from the coast to the interior of the continent [*Schlosser et al.*, 2008]. Along the escarpment between the coastal region and the interior plateau, local precipitation maxima are located on the windward side of topographical ridges.

Different mechanisms are important for the formation of precipitation along the marginal ice slopes of Antarctica and in the continental interior. In coastal regions, poleward moving moist air is deflected by the steep marginal ice slopes resulting in an air flow parallel to the terrain contours, which strongly influences the precipitation generation [*Bromwich*, 1988]. Further inland at higher elevations (> approximately 1000 m above sea level (masl)), direct orographic lifting is the dominant precipitation generation mechanism [*Bromwich*, 1988]. In the continental interior (> approximately 3000 masl), clear-sky precipitation, also known as "diamond dust," formed from ice nucleation in cold air is the most frequent form of precipitation [*Bromwich*, 1988]. However, high-precipitation events associated with synoptic-scale forcing are most relevant in terms of snow accumulation [*Bromwich*, 1988; *Reijmer and van den Broeke*, 2001].

High precipitation is always resulting from rapidly ascending low-level air containing a substantial amount of moisture [e.g., *Doswell et al.*, 1996, 1998]. The following basic ingredients assist the formation of high precipitation: (strong) vertical motion forcing, reduced static stability, and sufficient moisture supply. Synoptic-scale weather systems can affect all of these factors.

Indeed, the occurrence of high precipitation in coastal areas of DML is in general strongly influenced by synoptic-scale weather systems [*Bromwich*, 1988], such as transient extratropical cyclones [*Pfahl and Wernli*, 2012] in the circumpolar low-pressure trough and their associated frontal systems. These synoptic-scale weather systems strongly influence the advection of atmospheric moisture on a large spatial scale as well as the local stability and areas of strong uplift, for example, within warm conveyor belts of extratropical cyclones [*Pfahl et al.*, 2014]. The synoptic precipitation forcing can further constructively interact with the local orography to enhance precipitation even more [e.g., *Doswell et al.*, 1996, 1998]. At the eastern side of cyclones affecting DML, northerly to northeasterly winds prevail resulting in a pronounced onshore flow of low-level moist air, which is rapidly orographically lifted and cooled [*Schlosser et al.*, 2008].

In addition, the persistence and stationarity of weather systems plays an important part in the amplitude of high-precipitation events. Persistent weather patterns ensure sustained moisture supply to a specific area over several days and, hence, large precipitation accumulations. Persistent weather patterns are typically concomitant with high-amplitude waves in the upper level flow and blocking anticyclones, which can lock the phase of such waves. These persistent weather situations typically correspond to the negative phase of the Southern Annular Mode [*Marshall*, 2003; *Schlosser et al.*, 2011], which is regarded as the dominant mode of atmospheric variability in the Southern Hemisphere.

In the interior high-plateau region of DML, synoptically induced high-precipitation events occur episodically and are in general rare [*Noone et al*., 1999; *Schlosser et al*., 2010a]. However, these rare high-precipitation events contribute more to the total snow accumulation than the small events [*Reijmer and van den Broeke*, 2003]. The atmospheric conditions leading to high precipitation in the interior of DML have been widely investigated mostly on the basis of individual case studies [e.g., *Noone et al*., 1999; *Reijmer and van den Broeke*, 2001; *Birnbaum et al*., 2006; *Schlosser et al*., 2010a, 2010b; *Gorodetskaya et al*., 2013]. *Noone et al*. [1999] analyzed precipitation over DML's interior in 1979–1997 and performed case studies for two high-precipitation events, based on the European Centre for Medium-Range Weather Forecasts (ECMWF) reanalysis data (ERA; 1979–1993) and ECMWF operational analyses (1994–1997). They found that the high-precipitation events were associated with a pattern of an amplified upper level wave with a surface cyclone over the Weddell Sea and a blocking anticyclone over the South Atlantic. This synoptic pattern resulted in an enhanced poleward flow over DML, and the advection of warm and moist air masses from lower latitudes into the interior of DML was, thus, enhanced. *Reijmer and van den Broeke* [2001] found that a similar synoptic-scale pattern led to a high-precipitation event at Kohnen Station, located in the interior high-plateau region of DML (Figure 1), in May 1998.

Birnbaum et al. [2006] investigated the synoptic weather situations associated with high precipitation at Kohnen Station during the summers from 2001 to 2004. Using observations, satellite images, and ECMWF operational forecasts and analyses they grouped the weather situations into three categories: (i) cyclones over the Weddell Sea move eastward and associated occluding fronts reach the high-plateau region of DML; (ii) cyclones or secondary cyclones, which formed to the east of Kohnen Station, move westward (retrograde) and related fronts reach the plateau; (iii) upper level low situated to the west of Kohnen Station leads to large-scale lifting of moist air and, thus, cloud formation and snowfall on the plateau. Category (i) was the most frequent weather situation associated with high precipitation at Kohnen Station.

Schlosser et al. [2010a] identified frequently recurring synoptic situations associated with approximately 50 high-precipitation events at Kohnen Station in 2001–2006. Their study is based on data from the Antarctic Mesoscale Prediction System (AMPS) [*Powers et al*., 2003, 2012], which employed a polar-modified version of the fifth-generation Pennsylvania State University-National Center for Atmospheric Research Mesoscale Model (Polar MM5). *Schlosser et al*. [2010a] emphasized the importance of blocking anticyclones and correspondingly amplified Rossby waves for high precipitation at Kohnen Station. They further argued that these blocking situations require strong cyclogenesis over the Weddell Sea or over parts of the South Atlantic to the north of western DML. According to *Schlosser et al*. [2010a], high precipitation at Kohnen Station is in large part not directly related to the cyclones' frontal systems, but rather to orographic lifting of relatively warm and moist air advected from lower latitudes in a northwesterly to northeasterly flow between the cyclone and the blocking anticyclone. Such meridionally amplified Rossby waves associated with atmospheric blocking are often preceded by an upstream Rossby wave train [e.g., *Altenhoff et al*., 2008; *Sprenger et al*., 2013].

In the interior of East Antarctica to the east of Kohnen Station, periods characterized by anomalously high temperatures and increased atmospheric moisture are also often associated with blocking [e.g., *Enomoto et al*., 1998; *Hirasawa et al*., 2000, 2013]. Using the example of a strong blocking event that occurred over East Antarctica in June 1997, *Hirasawa et al*. [2000] stressed the importance of blocking concerning the anomalous weather conditions as observed at the high-altitude Dome Fuji Station. During the event, a strong blocking ridge developed over East Antarctica at the leading edge of a quasi-stationary Rossby wave train. This blocking ridge was associated with an enhanced poleward geostrophic wind along its upstream flank and, thus, enhanced poleward heat and moisture transport from lower latitudes into the interior of East Antarctica.

The research on atmospheric conditions concomitant with high precipitation in DML tended to focus on case studies. Our primary objective in this paper is to investigate the large-scale atmospheric environment that has contributed to high precipitation in DML from a climatological perspective. This climatological analysis includes a consideration of the statistical significance of the anomalous synoptic patterns concomitant with high precipitation in DML.

We analyze high precipitation in the relatively wet, low-altitude coastal region of DML and in the dry, high-altitude interior: i.e., at Halvfarryggen ice dome (71.2°S, 6.7°W), located in the hinterland of Neumayer Station at an elevation of approximately 700 masl, and at Kohnen Station (75°S, 0.1°E; 2892 masl) (Figure 1).

Halvfarryggen is a potential ice core drilling site within the International Partnerships in Ice Core Sciences, and Kohnen Station is a deep ice core drilling site in the framework of the European Project for Ice Coring in Antarctica [*EPICA Community Members*, 2006].

More specifically, for all high-precipitation events that occurred at each of these two locations during 1979–2009 and for all cooccurring events at both locations, we ask the following questions:

1. How anomalous were the moisture fluxes that resulted in the high-precipitation events and what were their spatial extents and their orientations relative to the local orography?
2. What was the upper level flow configuration at the time and prior to the high-precipitation events?
3. Were cyclones present during or prior to the events and, if yes, where were these cyclones located?
4. Were blocking anticyclones present during or prior to the events and, if yes, where were these blocks located?

To answer these questions, we use atmospheric reanalysis data from the ERA-Interim project [*Dee et al*., 2011] for 1979–2009 and objective climatologies of surface cyclones and blocking anticyclones [*Wernli and Schwierz*, 2006; *Schwierz et al*., 2004].

This paper further includes a comprehensive comparison of high precipitation in ERA-Interim with (i) high-resolution AMPS precipitation data and (ii) measured surface height changes from automatic weather stations (AWSs) located near Halvfarryggen and Kohnen Station, deployed by the Institute for Marine and Atmospheric Research Utrecht (IMAU), Utrecht University. The limitations of such a comparison are discussed.

2. Data and Methods

2.1. ERA-Interim Data

Our investigations are mainly based on the global ERA-Interim data set [*Dee et al*., 2011] for 1979–2009. The advantage of using reanalysis data is that they are globally available with high temporal resolution and that atmospheric circulation patterns, such as extratropical cyclones and blocking anticyclones, are well constrained by observations. ERA-Interim data are available every 6 h and were interpolated to a $1° \times 1°$ latitude-longitude grid (originally available with a T255 spectral resolution). In this study, ERA-Interim was used (i) to identify days with high precipitation at Halvfarryggen and Kohnen and (ii) to describe the associated large-scale atmospheric circulation.

2.1.1. Precipitation Data

The ability of ERA-Interim to represent Antarctic precipitation is not well known. Data from reanalyses should in general be treated with some caution, and Antarctica is a particularly challenging place for reanalyses simulations of precipitation [*Bromwich et al*., 2011], especially because it is such a data-sparse region.

ERA-Interim precipitation data agree well with independent satellite observations of precipitation over Antarctica, i.e., observations of snow precipitating through the atmosphere from the Cloud Profiling Radar on CloudSat [*Boening et al*., 2012; *Palerme et al*., 2014]. *Nicolas and Bromwich* [2011] and *Bromwich et al*. [2011] argued that the ERA-Interim data set provides the most realistic depiction of precipitation variability in high southern latitudes since 1989, compared to other contemporary reanalyses. *Cohen and Dean* [2013] evaluated how well ERA-Interim and the National Centers for Environmental Prediction/Department of Energy Atmospheric Model Intercomparison Project 2 reanalysis (NCEP 2) represent precipitation over the Antarctic Ross Ice Shelf on synoptic time scales by comparing precipitation data from these two reanalyses with snow accumulation measurements from AWSs. They found that ERA-Interim reproduces more precipitation events and also produces more precipitation per event than NCEP 2.

Precipitation data from ERA-Interim are entirely based on the underlying physical model's representation of hydrological processes, because precipitation forecasts are not directly constrained by precipitation observations [*Dee et al*., 2011]. Some of the problems with the representation of hydrological processes as they were found in the ECMWF ERA-40 data set were eliminated in ERA-Interim, owing to substantial improvements of the physical model and data assimilation techniques [*Andersson et al*., 2005; *Uppala et al*., 2008].

We analyzed 6-hourly ERA-Interim total precipitation forecast fields (in mm, where 1 mm of precipitation is the equivalent of 1 kg of water per m^2), i.e., the sum of large-scale precipitation, convective precipitation, and

Table 1. ERA-Interim Precipitation at Halvfarryggen and Kohnen Grid Points in 1979–2009

	Halvfarryggen	Kohnen
Cumulated precipitation (in mm) per year	726.0	115.8
95th percentile of daily precipitation sum (in mm d^{-1})	15.5	2.6
Maximal daily precipitation sum (in mm d^{-1})	59.9	12.5

snowfall. In this study, we give the total quantity for a certain time interval, typically for 1 day (in mm d^{-1}; denoted daily precipitation sum). For the ERA-Interim Halvfarryggen grid point (71°S, 7°W) and Kohnen grid point (75°S, 0°E), daily precipitation sums were computed (denoted ERA-I-P); the locations of the two grid points are indicated in Figure 1a.

2.1.2. Definition of High-Precipitation Events

We used ERA-Interim precipitation data to define high-precipitation days and events. A day with a daily precipitation sum exceeding a prescribed local precipitation threshold was defined as a high-precipitation day. High-precipitation events were defined as consecutive high-precipitation days separated by at least 1 day. We set two criteria for the selection of the ERA-Interim precipitation threshold: (i) for reasons of compatibility the threshold should be similar to that used by *Schlosser et al.* [2010a] and (ii) the threshold should be "locally extreme" (e.g., ≥95th percentile) to capture only synoptically induced precipitation.

Schlosser et al. [2010a] analyzed precipitation data in 2001–2006 from the AMPS employing Polar MM5. They applied for Kohnen a precipitation threshold of 1.6 mm d^{-1}. Of all days analyzed in their study, 4% had daily precipitation sums greater than this threshold. *Schlosser et al.* [2010a] referred to their precipitation threshold as rather high, which would ensure that only precipitation events associated with synoptic systems are considered.

For Kohnen, we applied a similar threshold in terms of precipitation frequency and defined high-precipitation days as those days when ERA-I-P was greater than or equal to the local 95th percentile (P95) of all precipitation days. The 95th percentile corresponds to 2.6 mm d^{-1} (Table 1). This value is considerably higher than the 1.6 mm d^{-1} threshold by *Schlosser et al.* [2010a], but ERA-I-P data for Kohnen exhibit a systematic high bias compared to AMPS precipitation data (see section 3.1). This bias in ERA-I-P data for Kohnen is in line with *Ye et al.* [2007], who found a positive bias in atmospheric total precipitable water over the Antarctic interior in ECMWF operational analysis data.

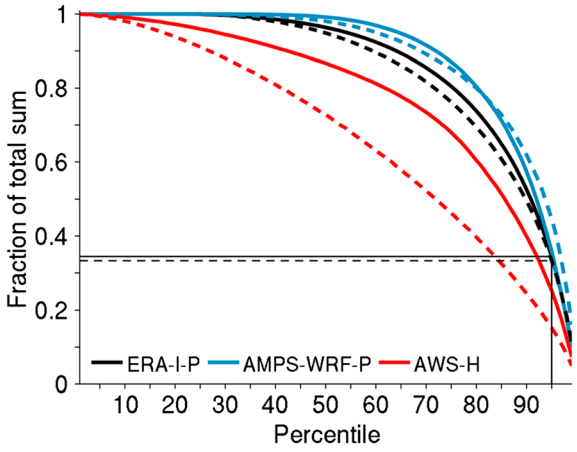

Figure 2. Distributions of ERA-I-P for Halvfarryggen (black solid line) and Kohnen (black dashed line) grid points from 1 January 1979 to 31 December 2009; AMPS-WRF-P distributions for Halvfarryggen (blue solid line) and Kohnen (blue dashed line) grid points from 7 March 2006 to 31 December 2009; distributions of AWS-H at AWS 11 (red solid line) on Halvfarryggen and at AWS 9 (red dashed line) at Kohnen Station between 18 January 2007 and 31 December 2009 and between 29 December 1997 and 31 December 2009, respectively. The *x* axis gives the precipitation (accumulation) percentile, and the *y* axis indicates the cumulated sum of all values above the respective percentile relative to the total sum of the variable. The value for P95 of ERA-I-P for Halvfarryggen (Kohnen) grid point is marked by the solid (dashed) horizontal line.

Daily precipitation values at Kohnen greater than or equal to P95 resulted in 33.3% of the total cumulated precipitation at Kohnen in 1979–2009, and at Halvfarryggen in 34.4% (Figure 2). Thus, for Halvfarryggen the same percentile threshold as for Kohnen was used. The P95 threshold for Halvfarryggen is 15.5 mm d^{-1} and, thus, almost 6 times higher than the threshold for Kohnen (2.6 mm d^{-1}) (Table 1).

A high-precipitation event at Halvfarryggen (i.e., the first day of consecutive high-precipitation days separated by at least 1 day) corresponds to a high-precipitation event at Kohnen in 33% of the cases. The day after (before) a high-precipitation event at Halvfarryggen corresponds to a high-precipitation event at

Kohnen in 17% (9%) of the cases, and the percentages decrease with increasing temporal lags. The horizontal distance between Halvfarryggen and Kohnen Station is approximately 500 km. It is therefore reasonable that a high-precipitation event at Halvfarryggen and an event at Kohnen are associated with the same synoptic weather situation, but separated by one or more days. However, because the percentage is highest for no lag, we consider in the sample of cooccurring high-precipitation events at Halvfarryggen and Kohnen only those dates when high precipitation at Halvfarryggen and at Kohnen occurred at the same day. This, however, implies that this sample is biased toward large synoptic systems (>500 km in scale).

2.1.3. Variables for Describing the Large-Scale Atmospheric Environment

To quantify the large-scale moisture flux associated with high precipitation at Halvfarryggen and Kohnen in a Eulerian framework, we computed the vertically integrated water vapor transport (IVT), indicating the direction as well as the magnitude (in kg $m^{-1} s^{-1}$). The primary parameters in the computation of IVT are the zonal and meridional wind components as well as the specific humidity at different levels of the atmosphere; the specific humidity was calculated from the same atmospheric model as the precipitation fields. For details on the computation of IVT we refer to *Lavers et al*. [2012]. Furthermore, for the Halvfarryggen and Kohnen grid points, we defined high-IVT days as those days when the daily-mean IVT magnitude was greater than or equal to the local 95th percentile. The P95 value of the daily-mean IVT magnitude at Halvfarryggen is 104.0 kg $m^{-1} s^{-1}$ and, thus, more than 7 times higher than the corresponding P95 value for Kohnen (14.4 kg $m^{-1} s^{-1}$). This ratio is approximately the same as the ratio of the P95 value of ERA-I-P at Halvfarryggen and the P95 value of ERA-I-P at Kohnen.

To describe the large-scale upper tropospheric dynamics associated with high-precipitation events at Halvfarryggen and Kohnen, we analyzed fields of upper level potential vorticity (PV) on isentropic surfaces, i.e., on the 325 K isentropic surface for the seasons December-January-February (DJF), March-April-May (MAM), September-October-November (SON), and on the 320 K isentropic surface for June-July-August (JJA).

To investigate the link between extratropical cyclones and the occurrence of high precipitation in DML, the objective surface cyclone detection algorithm of *Wernli and Schwierz* [2006] was applied to the mean sea level pressure (MSLP) fields. In this scheme, a cyclone is defined as the finite area that surrounds a local MSLP minimum bounded by a closed MSLP contour line with a prescribed minimum (maximum) length of 100 km (7500 km). The output of the algorithm is a binary field for each time step that indicates the presence of cyclones at each grid point. Cyclones over ERA-Interim orography exceeding 1500 masl were discarded because of the considerable extrapolation that was necessary for the MSLP computation over high mountains.

Complementarily, to analyze atmospheric blocking associated with high precipitation in DML, the PV-based blocking algorithm developed by *Schwierz et al*. [2004] was applied. This algorithm identifies the location and spatial extent of blocks with a lifetime exceeding 5 days taking into account the three-dimensional structure of a block; i.e., it detects vertically coherent positive PV anomalies (for the Southern Hemisphere) at tropopause altitudes. Similar to the cyclone identification scheme, the output of the blocking algorithm is a binary field for each time step indicating the presence of blocking at each grid point.

For the variables IVT, upper level PV on isentropic surfaces, surface cyclone frequency, and blocking frequency, we computed composites for high-precipitation events at Halvfarryggen or Kohnen as well as for cooccurring high-precipitation events at both sites. For the composite analyses only the first day of each event was considered. In addition, we computed composites for the 4 days preceding a high-precipitation event.

We tested the statistical significance of the composites with regards to a climatological state using a Monte Carlo method, where the composited fields were compared to 500 random composites which contain the same number of events and consider the seasonal distribution of individual events in the original composites. To generate a random date, we changed randomly the day of the event (between −10 days and +10 days around the day of the event) and the year of the event (between 1979 and 2009), but the month of the event was not changed.

2.2. Data for Comparison With ERA-Interim Precipitation Data

The overall sparseness of in situ and satellite measurements in Antarctica makes the evaluation of precipitation from reanalyses difficult. For comparison with ERA-Interim precipitation data, we used

measured surface height changes from the IMAU AWSs located near Halvfarryggen and Kohnen Station as well as model-based precipitation data from the AMPS in this study.

2.2.1. AMPS Precipitation Data

The current AMPS setup employs a version of the Weather Research and Forecasting Model (WRF) [*Skamarock et al*., 2008] optimized for polar ice sheets (Polar WRF). Polar WRF gets its first-guess fields and boundary conditions from the Global Forecast System weather forecast model produced by NCEP. *Powers et al*. [2003, 2012] give a useful summary of the AMPS system and the products provided.

We analyzed AMPS-WRF precipitation data available for 48°S-90°S, 180°W-180°E and 7 March 2006 to 31 December 2009. The data have a 3-hourly temporal resolution and range in horizontal resolution from 20 km (until November 2008) to 15 km (since November 2008). Based on this data, we computed daily precipitation sums for the AMPS-WRF grid points closest to Halvfarryggen and Kohnen Station (in mm d^{-1}; denoted AMPS-WRF-P); the locations of the two AMPS-WRF grid points are indicated in Figure 1b. Note the distinctively lower resolution of the surface topography in the ERA-Interim (Figure 1a), which may compromise the ability of the model to quantitatively reproduce precipitation events. Analogous to the definition of high-precipitation days in ERA-Interim data, high AMPS-WRF-P days were defined as those days when AMPS-WRF-P was greater than or equal to P95 of AMPS-WRF-P.

2.2.2. AWS Measurements

Measuring precipitation in Antarctica is an unsolved problem, which is mainly due to the problem of differentiating between falling precipitation and blowing snow [*Schlosser et al*., 2008]. Snow height changes, measured using a sonic height sensor mounted on the AWS, serve as an indicator for snow accumulation changes [*Reijmer and van den Broeke*, 2001]. Measured snow height changes include, besides snowfall, processes such as wind erosion and deposition, densification of the snowpack, and sublimation. These processes are generally not easy to differentiate in the time series of measured snow height changes [*Reijmer and van den Broeke*, 2003]. Due to the complex effects of wind, which can lead to both an increase and a decrease of snow accumulation, a determination of possible biases in the model-based precipitation data is virtually impossible with AWS data [*Cohen and Dean*, 2013]. *Schlosser et al*. [2008] further suggested that measured surface height changes from AWSs have to be used cautiously when used to reconstruct precipitation. However, AWS data are indispensible to estimate the surface mass balance at a given site and the seasonal changes in snow accumulation.

The IMAU operates different AWSs in DML [*Reijmer and van den Broeke*, 2003]. In this study, we analyzed instrument height data from AWS 11 (71.2°S, 6.8°W; approximately 690 masl) on Halvfarryggen and AWS 9 (75°S, 0°E; approximately 2900 masl) at Kohnen Station (Figure 1a). Based on 2-hourly to 1-hourly resolved instrument height data from the AWSs, we computed time series of positive daily snow height changes for each AWS (in m snow; denoted AWS-H). Data are available for 18 January 2007 to 31 December 2009 (29 December 1997 to 31 December 2009) in case of AWS 11 (AWS 9). Analogous to the model-based precipitation data, high AWS-H days at AWS 11 and AWS 9 were defined as those days when AWS-H was greater than or equal to P95 of AWS-H.

To estimate the influence of wind on snow accumulation at AWS 11 and AWS 9, we first computed time series of daily-mean wind speed measured at the AWS (denoted AWS-WS). Assuming that for substantial snowdrift it needs a certain wind speed, we then applied for both AWS sites a wind speed threshold of 5 m s^{-1} to identify days with no wind or days with low wind speed on which snowdrift was less likely (i.e., AWS-WS <5 m s^{-1}) and days with enhanced wind speed on which snowdrift was more likely (i.e., AWS-WS ≥ 5 m s^{-1}). The wind speed categories will be used later on to scrutinize the effect of high wind speeds on wind reworking in the AWS-H data.

3. Results

3.1. ERA-Interim Precipitation Data Compared to Other Data Sets

In this section, we compare ERA-I-P data for Halvfarryggen and Kohnen with the corresponding AMPS-WRF-P and AWS-H data, with the aim of providing a systematic comparison of ERA-Interim precipitation data over DML with other model and observational data sets that were used in previous studies to analyze high-precipitation and high snow accumulation events, respectively, in DML [e.g., *Schlosser et al*., 2010; *Reijmer and van den Broeke*, 2003].

Distributions of ERA-I-P, AMPS-WRF-P, and AWS-H data for Halvfarryggen and Kohnen are compared against each other in Figure 2, where the abscissa indicates the percentile (ranging from the 1st percentile to the 99th percentile) and the ordinate gives for each variable the cumulated sum of all values above the respective percentile relative to the total sum of the variable. The distributions of ERA-I-P for Halvfarryggen and Kohnen are overall comparable to the corresponding AMPS-WRF-P distributions. Daily precipitation values at Halvfarryggen (Kohnen) greater than or equal to P95 resulted in 34.4% (33.3%) of the total precipitation sum at Halvfarryggen (Kohnen) in ERA-Interim, and in 35.8% (44.7%) in AMPS-WRF. The absolute differences between the values of the ERA-I-P distribution and the values of the AMPS-WRF-P distribution are larger on average for Kohnen (4.5%) compared to Halvfarryggen (2.7%). In general, comparability is limited between the ERA-I-P distribution for Halvfarryggen and the AWS-H distribution for AWS 11 on Halvfarryggen. The ERA-I-P distribution for Kohnen and the AWS-H distribution for AWS 9 at Kohnen Station differ even more strongly. In summary, the distributions of ERA-I-P for Halvfarryggen and Kohnen and the corresponding distributions of AMPS-WRF-P are in general comparable, whereas the comparability between the distributions of ERA-I-P and the corresponding distributions of AWS-H is limited. For the AWS-H data a generally broader distribution of daily accumulation values is found than for precipitation, suggesting that wind redistribution leads to a higher variability in layer thicknesses.

The conclusions from Figure 2 are consistent with Figure 3 which shows scatterplots of the different variables. The ERA-I-P and AMPS-WRF-P time series for Halvfarryggen are well correlated, and the linear correlation coefficient between both variables is 0.84 (Figure 3a). The same is true for Kohnen with a correlation coefficient of 0.75 (Figure 3b); however, ERA-I-P data for Kohnen exhibit a systematic high bias compared to the corresponding AMPS-WRF-P data. The correlations between the ERA-I-P and AWS-H time series are much weaker. For Halvfarryggen the linear correlation coefficient is 0.32 and for Kohnen 0.07 (Figures 3c and 3d). The linear correlations between AMPS-WRF-P and AWS-H are comparable to the correlations for the reanalysis data: 0.37 for Halvfarryggen and 0.07 for Kohnen.

The weak correlation between ERA-I-P or AMPS-WRF-P and the snow accumulation observations was at least partly to be expected, because it is generally difficult to assess how much of the accumulation is due to snowfall and how much is due to snowdrift [e.g., *Reijmer and van den Broeke*, 2003]. Moreover, the relationship between change of snow height and wind speed on Halvfarryggen is different from the relationship at Kohnen Station: the linear correlation coefficient between the AWS-H and the AWS-WS time series is 0.4 for AWS 11 (Halvfarryggen) and 0.08 for AWS 9 (Kohnen Station).

The correlation between ERA-I-P and AWS-H at Halvfarryggen improves (0.43 compared to 0.32 for all days) if only days with no wind or days with low wind speed at the AWS are considered when snowdrift was unlikely (blue downward pointing triangles in Figure 3c). The correlation at Kohnen does not improve when only considering days with no wind or days with low wind speed.

An important limitation of the model-based data is that the orography is in general not realistically represented in the model due to the relatively coarse model grid resolution. Halvfarryggen, for example, is not realistically resolved in neither the ERA-Interim model (Figure 1a) nor in the AMPS-WRF model (Figure 1b). Thus, a comparison between coarse-resolution model-based precipitation data at Halvfarryggen and point measurements of snow height changes at an AWS is intrinsically limited, because on the windward side of topographical ridges (such as Halvfarryggen) precipitation and, thus, snow accumulation is higher compared to the surroundings [*Schlosser et al*., 2008].

Weak correlations between ERA-Interim precipitation and AWS accumulation are found for all days, and it is interesting to see whether the days in the AWS-H records with high snow accumulation correspond to high-precipitation days in the corresponding ERA-I-P records. For this comparison, we firstly determined the dates with high precipitation in the reanalysis and the dates with high snow accumulation at the AWSs, and the absolute number of common days was then divided by the maximum possible intersection of high ERA-I-P days and high AWS-H days; i.e., a value of 1 indicates that all days are coincident. We find that the relative frequency of days with high ERA-I-P values and high AWS-H values is comparatively low for both Halvfarryggen and Kohnen, namely 0.16 and 0.09. In contrast, the relative frequency of days common to both high ERA-I-P days and high AMPS-WRF-P days is much higher: 0.61 for Halvfarryggen and 0.60 for Kohnen.

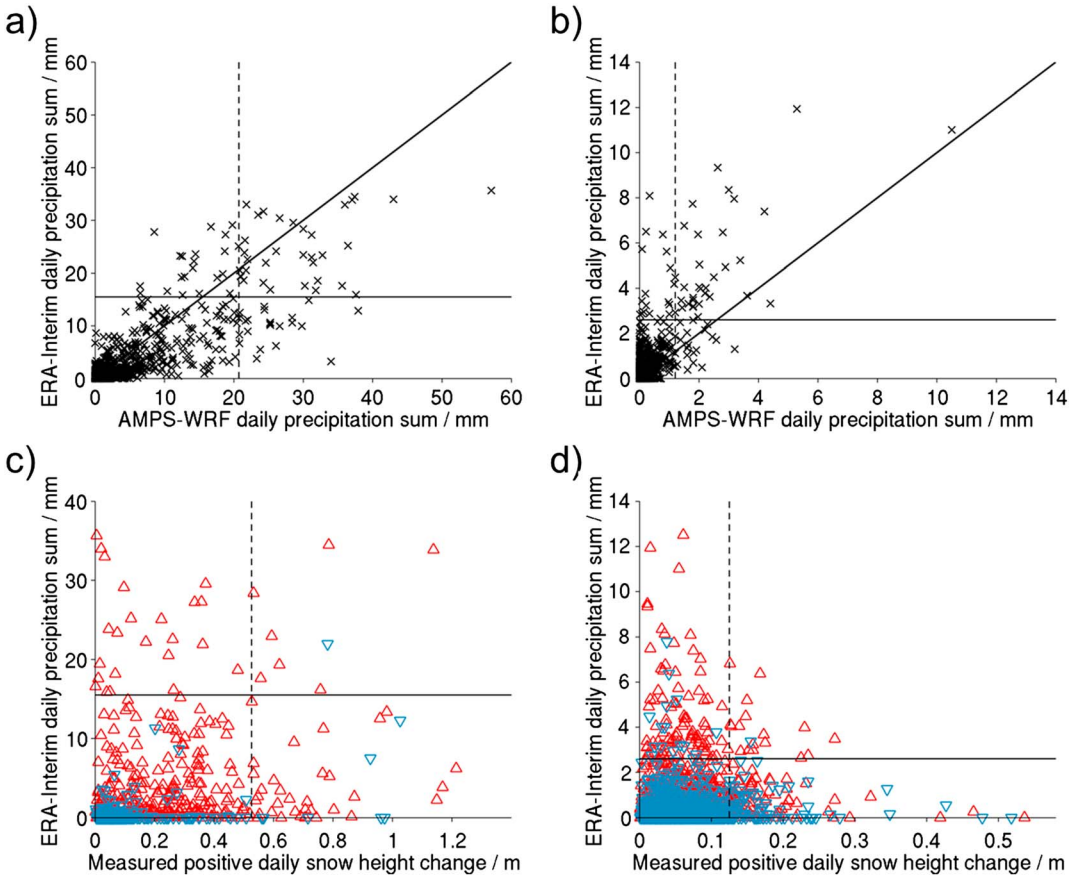

Figure 3. Scatterplots of daily precipitation sums between 7 March 2006 and 31 December 2009 obtained from AMPS-WRF (mm; *x* axis) and from ERA-Interim (mm; *y* axis) for the (a) Halvfarryggen and (b) Kohnen grid points; the 1:1 line is drawn as a reference in Figures 3a and 3b. Scatterplots for measured positive snow height changes (m; *x* axis) and ERA-Interim daily precipitation sums (mm; *y* axis) for (c) AWS 11/Halvfarryggen grid point and (d) AWS 9/Kohnen grid point between 18 January 2007 and 31 December 2009 and between 29 December 1997 and 31 December 2009, respectively. In Figures 3c and 3d, days with no wind or days with low wind speed at the AWS are plotted as blue downward pointing triangles and days with enhanced wind speed are plotted as red upward pointing triangles (for the definition of the two wind speed classes applied here see section 2.2.2). In Figures 3a–3d, the P95 values of the respective variables are marked by the black solid and dashed lines.

To partly take into account the complex influence of wind on snow height changes at the AWSs, we computed statistics of the relative frequency of days common to both high ERA-I-P days and high AWS-H days after splitting the high AWS-H days according to the strength of the prevailing wind (see section 2.2.2). We do not find a significant improvement of the correspondence; however, the number of cases that fall into each category is low.

3.2. Characteristics of High Precipitation in DML Based on ERA-Interim

In the ERA-Interim data set, the annual precipitation sum for Halvfarryggen is more than 6 times higher than for Kohnen (Table 1), reflecting the precipitation decrease with increasing distance from the coast and elevation [*Schlosser et al*., 2008]. The maximum daily precipitation sum for Halvfarryggen is almost 5 times higher than for Kohnen. The percentage of days with no precipitation is higher for Kohnen (50%) compared to Halvfarryggen (42%). The standard deviation of logarithmic ERA-I-P at Halvfarryggen is similar to the standard deviation of logarithmic ERA-I-P at Kohnen.

According to our definition of high-precipitation days and events, 10.7 high-precipitation days and 7.7 high-precipitation events occurred per year at Halvfarryggen (Table 2); the corresponding values for Kohnen are with 9.2 days and 6.5 events comparable. *Schlosser et al*. [2010a] applied a slightly higher percentile-threshold for precipitation at Kohnen and identified 8.5 high-precipitation days per year.

Table 2. ERA-Interim High-Precipitation Days and Events at Halvfarryggen and Kohnen Grid Points in 1979–2009

	Halvfarryggen	Kohnen	Halvfarryggen and Kohnen[a]
Number of high-precipitation days per year	10.7	9.2	4.3
Percentage of days in DJF	18.7	23.9	22.7
Percentage of days in MAM	32.0	29.6	27.3
Percentage of days in JJA	22.4	23.2	27.3
Percentage of days in SON	26.9	23.2	22.7
Number of high-precipitation events per year	7.7	6.5	3.5

[a]Cooccurring high-precipitation days (events) at Halvfarryggen and Kohnen.

Cooccurring high-precipitation days at Halvfarryggen and Kohnen happened on average 4.3 days per year, corresponding to 3.5 events per year (Table 2). All of the top 10 precipitation days at Halvfarryggen belong to this sample; cooccurring high-precipitation days at Halvfarryggen and Kohnen comprise 100% (74%) of the top 10 (top 50) precipitation days at Halvfarryggen, and 70% (62%) of the top 10 (top 50) precipitation days at Kohnen.

The seasonality of high-precipitation days is greater for Halvfarryggen than for Kohnen (Table 2). At Halvfarryggen, high-precipitation days are most frequent during autumn (MAM) and least frequent during summer (DJF). A similar seasonal cycle was found by *Lenaerts et al.* [2012] for total snowfall over Antarctica, determined by computing the surface mass balance of the entire Antarctic ice sheet based on a regional atmospheric climate model forced by ERA-Interim. At Kohnen, occurrence frequencies of high-precipitation days are also highest during autumn (MAM) and lowest during winter (JJA) and spring (SON). However, the seasonality at Kohnen is weak, which is interestingly in line with the findings of *Reijmer and van den Broeke* [2003] who analyzed the seasonality of large snow accumulation events in DML based on AWS data.

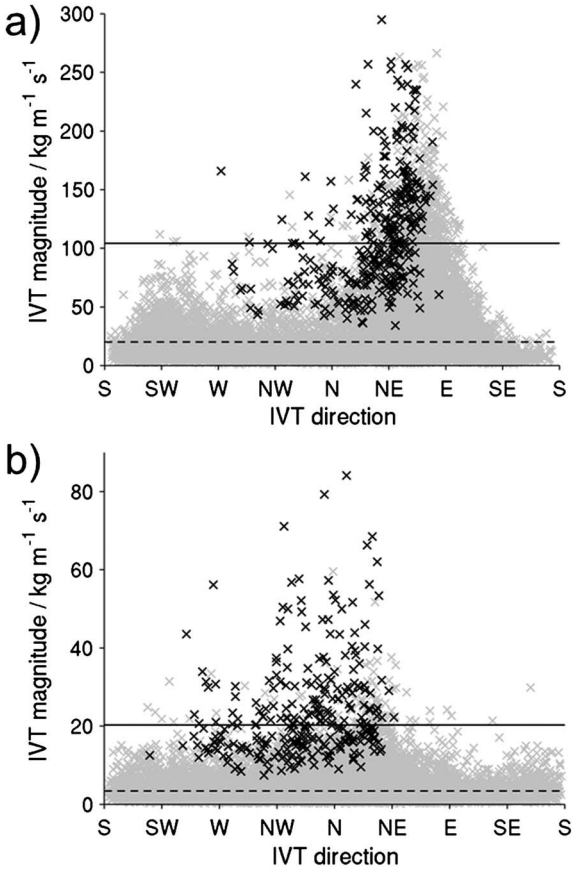

Figure 4. Daily-mean vertically integrated water vapor transport at (a) Halvfarryggen and (b) Kohnen grid points in 1979–2009. The *x* axis indicates the direction and the *y* axis shows the magnitude of the IVT in kg m^{-1} s^{-1}. Black cross symbols mark high-precipitation days and gray cross symbols mark the remaining days. For the IVT magnitude, the medians of the distributions for high-precipitation days (remaining days) are marked with the solid (dashed) lines in Figures 4a and 4b.

3.3. Large-Scale Moisture Flux Associated With High Precipitation in DML

Figure 4 shows the daily-mean IVT distributions for Halvfarryggen and Kohnen for all days in 1979–2009. The median IVT during high-precipitation days (remaining days) is 104.1 kg m^{-1} s^{-1} (20.1 kg m^{-1} s^{-1}) in case of Halvfarryggen (Figure 4a) and 20.2 kg m^{-1} s^{-1} (3.4 kg m^{-1} s^{-1}) in case of Kohnen (Figure 4b). Thus, for Halvfarryggen, the median of the IVT magnitude distribution for high-precipitation days is more than 5 times higher than for the remaining days, and almost 6 times for Kohnen.

The IVT distribution for Halvfarryggen reveals two preferred flow directions associated with high-IVT values: northeasterly to easterly for the highest-IVT values and southwesterly for the lower-IVT values (Figure 4a). These two preferred flow directions for high-IVT values

are approximately parallel to the local ERA-Interim orography (Figure 1a), which indicates that high-IVT values at Halvfarryggen generally occurred when the flow was parallel to the terrain contours. In contrast, high-precipitation days at Halvfarryggen do not necessarily correspond to high-IVT values, but rather correspond to the IVT with the strongest component perpendicular to the local orography. High-precipitation days at Halvfarryggen occurred during IVTs ranging from westerly over northerly to easterly directions, and most of the high-precipitation days occurred during a northeasterly IVT (Figure 4a). At Halvfarryggen, 95% of all high-precipitation days occurred during IVTs ranging from W to ENE and 56% of all IVT days above the 95th percentile (i.e., high-IVT days) at Halvfarryggen had flow directions in this range. Even though 40% of all high-IVT days at Halvfarryggen had flow directions between ENE and E, only 5% of all high-precipitation days at Halvfarryggen occurred during IVTs ranging from ENE to E. These percentages indicate that during IVTs ranging from W to ENE, and in particular during northeasterly IVT, the interaction of the moisture flux with the local orography at Halvfarryggen was more effective in producing high precipitation than during easterly IVT. This also explains why at Halvfarryggen only 50% of all high-IVT days, irrespective of the direction, correspond to high-precipitation days.

The location of Kohnen Station on the high-altitude interior plateau allows moisture fluxes from different directions (Figure 1). As a consequence, the IVT distribution for Kohnen reveals a broad range of flow directions for high-IVT values ranging from southwesterly over northerly to northeasterly directions, with a weak maximum at flow directions from northwesterly to northeasterly (Figure 4b). All high-precipitation days at Kohnen occurred during IVTs from these directions. Irrespective of the IVT direction, 80% of all high-IVT days at Kohnen resulted in high-precipitation days; and high-IVT days at Kohnen comprise 100% of the top 50 precipitation days, compared to 82% at Halvfarryggen. These results indicate that the dependence on the direction of the IVT was less pronounced in case of high precipitation at Kohnen compared to high precipitation at Halvfarryggen.

Figure 5 shows IVT composites for high-precipitation events at Halvfarryggen and Kohnen as well as for cooccurring high-precipitation events at Halvfarryggen and Kohnen (at the first day of the event). In all three cases, high-precipitation events were associated with statistically significant large-scale IVT patterns, indicating a pronounced poleward IVT over DML. Because of DML's steep orography, the advected moist air masses are then forced to rise, resulting in adiabatic cooling of the air, condensation of the water vapor in the air, and ultimately cloud formation and high precipitation. Overall, the IVT composites for high-precipitation events at Halvfarryggen (Figure 5a) are similar to the IVT composites for high-precipitation events at Kohnen (Figure 5b) with the exception that the IVT composites for Halvfarryggen are larger in amplitude and the significant areas extend further into the midlatitudes.

3.4. Synoptic-Scale Atmospheric Conditions

An amplified wave pattern characterizes the upper level flow during high-precipitation events at Halvfarryggen and Kohnen as well as during cooccurring high-precipitation events at Halvfarryggen and Kohnen (Figure 6). This statistically significant amplified wave pattern consists of a trough located at 35°W, a strong ridge downstream centered at 10°E, and a second trough downstream of the ridge located at 60°E. During high-precipitation events, Halvfarryggen was typically located on the eastern flank of the western upper level trough, between the trough and the ridge and, hence, in an area of northwesterly to northerly winds (Figure 6a). The composite of the upper level flow during high-precipitation events at Kohnen is very similar (Figure 6b). However, the ridge is slightly broader corresponding to a more westerly direction of the flow between the upstream trough and the ridge, and the statistically significant anomalies extend less into the midlatitudes.

At the surface, the upper level PV trough-ridge-trough pattern was associated with local maxima and minima in the cyclone frequency (Figure 7). During high-precipitation events at Halvfarryggen and Kohnen as well as during cooccurring high-precipitation events at Halvfarryggen and Kohnen, cyclone frequency was increased underneath the trough at 25°W to the west of DML over the Weddell Sea. The slight eastward shift of the surface cyclone with respect to the upper level trough is in line with the characteristic vertical tilt of a baroclinic system. The surface cyclone frequency maximum exceeds 70% for the high-precipitation events at Halvfarryggen (Figure 7a) and 50% for the high-precipitation events at Kohnen (Figure 7b). The cyclone frequency is statistically significantly decreased to the northeast of DML over the South Atlantic underneath the upper level ridge at 15°E. During events with high precipitation both at Halvfarryggen and at Kohnen the

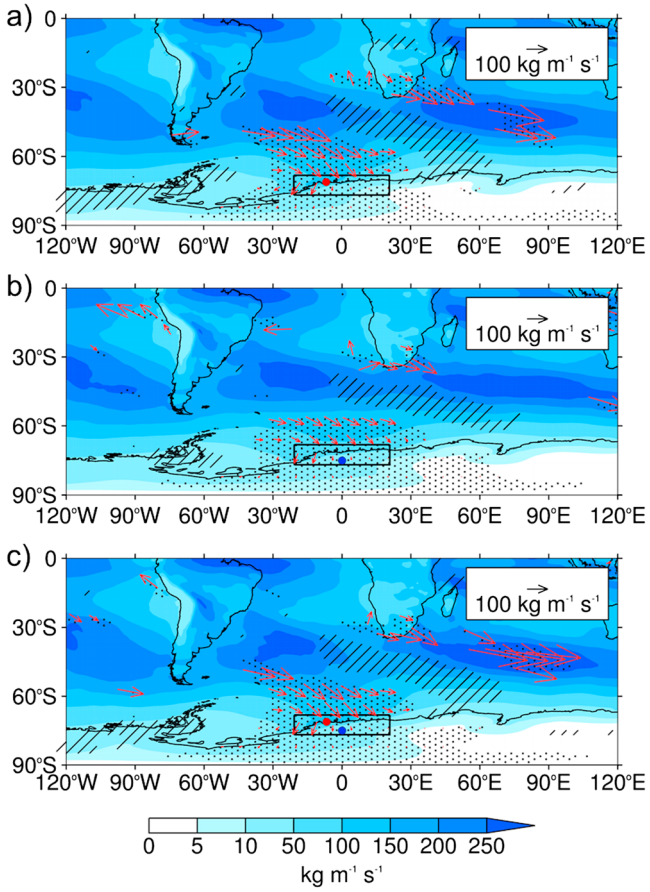

Figure 5. The color scheme indicates composite averages of the vertically integrated water vapor transport magnitude in kg $m^{-1} s^{-1}$ for high-precipitation events at (a) Halvfarryggen, (b) Kohnen, and for (c) cooccurring high-precipitation events at Halvfarryggen and Kohnen. Note the nonlinear color scale. Significantly positive (negative) composite averages at the 5% significance level are marked with dots (diagonal lines). Vectors indicate the direction (and magnitude) of statistically significant positive IVT. The domain shown in Figure 1 is outlined in Figures 5a–5c (black box), together with the locations of Halvfarryggen (red dot) and Kohnen Station (blue dot).

cyclone frequency in this area is between 0% and 10% (Figure 7c) and slightly higher in the Halvfarryggen (<20%) and Kohnen (<30%) composites. Downstream at approximately 70°E to 90°E underneath the downstream upper level trough, a second statistically significant maximum in the cyclone frequency is found, but cyclone frequencies are lower than over the Weddell Sea, exceeding 50%.

The upper level ridge located over the South Atlantic between 0° and 30°E corresponds to a statistically significant maximum in the blocking frequency during high-precipitation events at Halvfarryggen and Kohnen as well as during cooccurring high-precipitation events at Halvfarryggen and Kohnen (Figure 8). Blocking frequency maxima exceed in all three cases 14%. Overall, the blocking composites for Halvfarryggen and Kohnen are similar with the exception that the statistically significant areas of the composites for Kohnen reach slightly further into the continent. Blocking anticyclones effectively block or redirect transient extratropical cyclones. Hence, the high surface cyclone anomalies over the Weddell Sea (Figure 7) during high-precipitation events in DML are consistent with the anomalously high blocking frequencies over the South Atlantic (Figure 8). At the same time, *Schlosser et al.* [2010a] argued that these blocking situations over the South Atlantic require strong cyclogenesis over the Weddell Sea. Cyclonic systems are relevant for blocking formation and maintenance [e.g., *Shutts*, 1983] and to ensure the stationarity of the blocking anticyclone [*Altenhoff et al.*, 2008].

To assess how strongly the large-scale atmospheric patterns shown in Figures 5–8 depend on the precipitation threshold used to define high-precipitation events at Halvfarryggen (Kohnen), we computed the composites for local percentile-thresholds ranging from P75 up to P99 (not shown). These analyses indicate that our results are very robust in terms of the spatial patterns but the patterns vary in spatial extent and amplitude for other thresholds.

Furthermore, we defined two boxes based on the cyclone and blocking composites given in Figures 7 and 8 and then identified the 6-hourly time steps of all high-precipitation days at Halvfarryggen and Kohnen during which at least 25% of the grid cells of the respective box were located either within a cyclone or within a blocking anticyclone. Box 1 is located at 62°S-82°S, 52°W-7°W and comprises large parts of the Weddell Sea; Box 2 is situated over the South Atlantic at 53°S-73°S, 6°W-39°E. The boxes have the same size concerning the number of grid points.

In 82% of the total number of time steps of all high-precipitation days at Halvfarryggen, cyclones were present in Box 1 (Table 3); the frequency is lower for Kohnen with 66%. Blocking anticyclones were present in Box 2 in

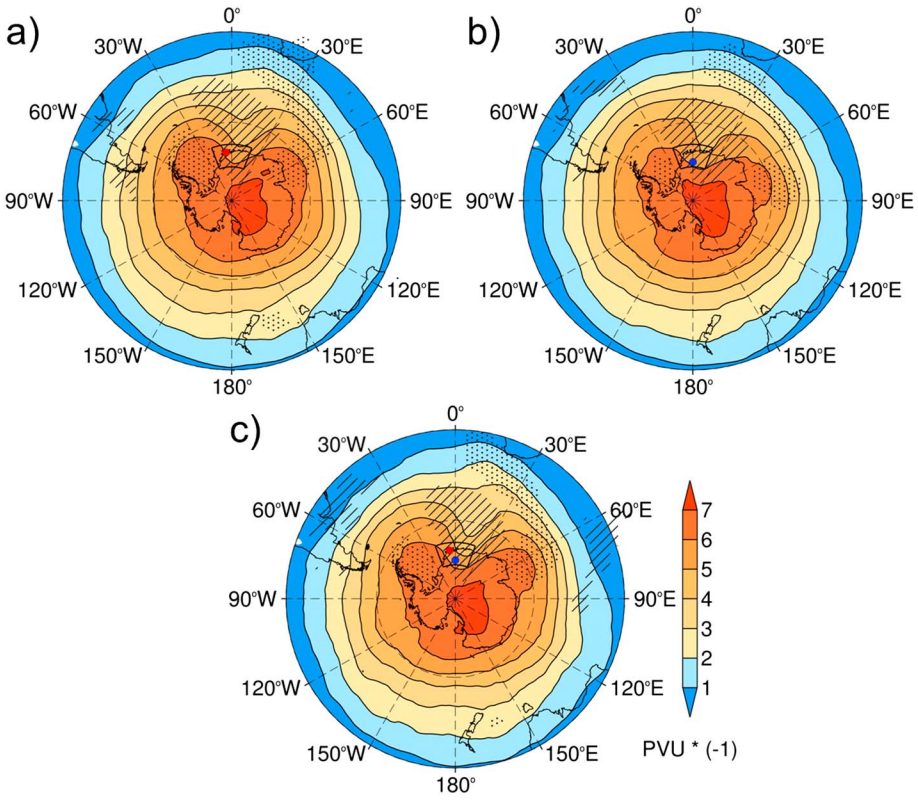

Figure 6. Analogous to Figure 5 but shown here are composites of the upper level potential vorticity on isentropic surfaces (325 K for DJF, MAM, SON, and 320 K for JJA) in potential vorticity units (PVU; 1 PVU = 10^{-6} m^2 s^{-1} K kg^{-1}) multiplied by −1. Significantly positive (negative) composites at the 5% significance level are marked with dots (diagonal lines). The domain shown in Figure 1 is marked in black.

23% of the total number of time steps of all high-precipitation days at Halvfarryggen and in 30% at Kohnen. These percentages depend on our requirement that at least 25% of the grid cells of the respective box were located within a cyclone or block. We consider this requirement to be suitable for two reasons: first, the frequency maxima of surface cyclones and blocking anticyclones in the composites (Figures 7 and 8) are smaller than the absolute counts of cyclones and blocks associated with high precipitation (Table 3) because the exact location of the synoptic systems varies from event to event. Second, the 25% threshold ensures that the cyclone (blocking) field affects a large area of the boxes. Cyclones have a mean radius of approximately 350 km to more than 800 km throughout their life cycle [*Wernli and Schwierz*, 2006]. The area of a cyclone (considered as a circle) with a radius of 350 km–800 km corresponds to 11%-59% (8%-40%) of the area of Box 1 (Box 2). Our 25% threshold is within this range. We examined how sensitive our results are on the selection of this threshold by computing percentages for both a lower threshold (≥20% of the number of grid cells) and a higher threshold (≥30%). We find that even though the percentages are slightly different our general conclusion remains the same: during high-precipitation days at Halvfarryggen and Kohnen the surface cyclone frequency was on average considerably higher in Box 1 than in Box 2, while the opposite is true for blocking frequency.

It is also interesting to look at the joint occurrence frequencies of cyclones and blocks in Boxes 1 and 2 during high-precipitation days at Halvfarryggen and Kohnen. The results are summarized in Table 4. We distinguish between the following four configurations: (i) cooccurrence of cyclones in Box 1 and blocking in Box 2, (ii) cyclones in Box 1 and no blocking in Box 2, (iii) no cyclones in Box 1 but blocking in Box 2, and (iv) neither cyclones in Box 1 nor blocking in Box 2. Note that configuration (iv) does not necessarily imply that no synoptic feature was present at these days. It is rather possible that a day is categorized as such because of the prescribed cyclone and blocking detection criteria of the algorithms used as well as because of our requirement that at least 25% of the grid cells of the respective box were

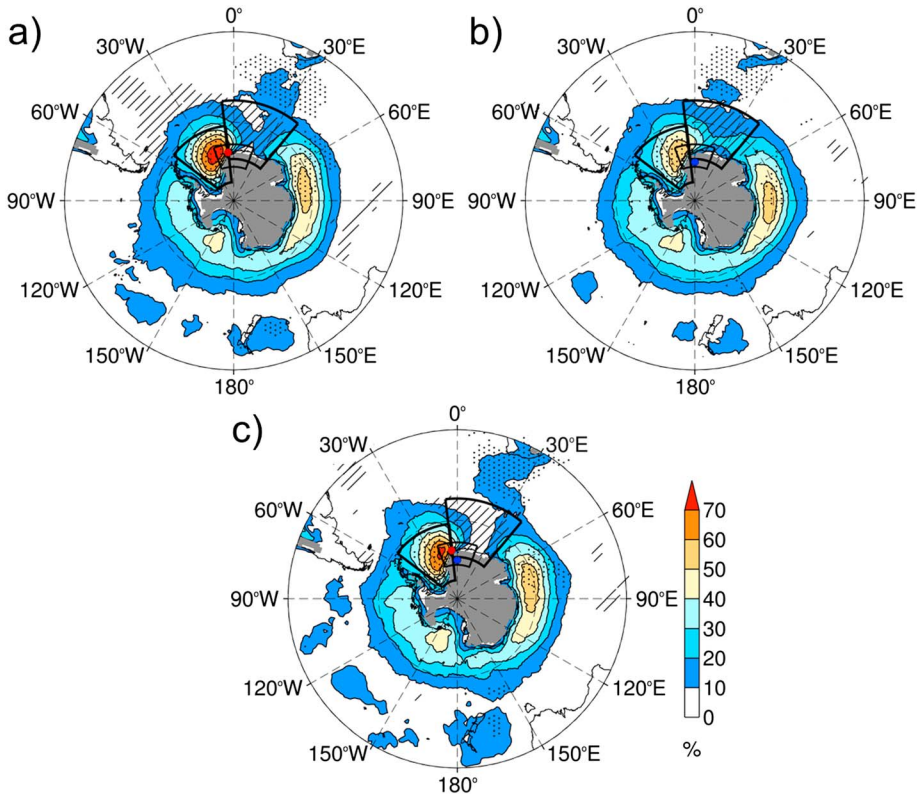

Figure 7. Analogous to Figure 5 but shown are composites of the surface cyclone frequency in %; gray areas indicate regions where the ERA-Interim orography exceeds 1500 masl. Dots (diagonal lines) indicate areas where the composites are significantly positive (negative) at the 5% significance level. The domain shown in Figure 1, Box 1 located at 62°S-82°S, 52°W-7°W, and Box 2 situated at 53°S-73°S, 6°W-39°E are marked in black (see section 3.4).

located within a cyclone or a block. For Halvfarryggen, the most frequent configuration was a cyclone located over the Weddell Sea and no blocking downstream (64%). Of secondary importance were the configurations cyclone and blocking (18%), blocking alone (6%), and neither cyclone nor block (12%). For Kohnen, the most frequent configuration was also a cyclone located over the Weddell Sea (47%); second to that is the concurrent presence of a cyclone and a block (19%), followed by blocking alone (11%) and days without a cyclone nor a block (23%).

Tables 3 and 4 suggest that for high precipitation at Halvfarryggen the presence of cyclones over the Weddell Sea was more important than for high precipitation at Kohnen. On the other hand, for high precipitation at Kohnen, the occurrence of blocking over the South Atlantic was more important than it was for high precipitation at Halvfarryggen. For cooccurring high precipitation at Halvfarryggen and Kohnen, the importance of blocking over the South Atlantic was higher than in case of high precipitation at Kohnen alone. For cooccurring high-precipitation days at Halvfarryggen and Kohnen, the configuration of cooccurring cyclones in Box 1 and blocking in Box 2 was present during a higher percentage of time steps (29%) than in case of high precipitation at Halvfarryggen (18%) or at Kohnen (19%) alone.

We have shown that the sample of cooccurring high-precipitation days at Halvfarryggen and Kohnen includes the majority of the highest-precipitation days at each location. The question arose, which of the aforementioned configurations was prevailing during these days. Hence, we analyzed the prevailing configurations during the top 10 (top 50) precipitation days at Halvfarryggen and Kohnen. The results are summarized in Table 5. The majority of the highest-precipitation days at Halvfarryggen were associated with the following two configurations: cooccurrence of cyclones in Box 1 and blocking in Box 2 (5 and 12 cases), as well as cyclones in Box 1 however no blocking in Box 2 (4 and 25 cases). Similar results are found for the highest-precipitation days at Kohnen; in addition, the configuration of no cyclones in Box 1 but blocking in Box 2 was important.

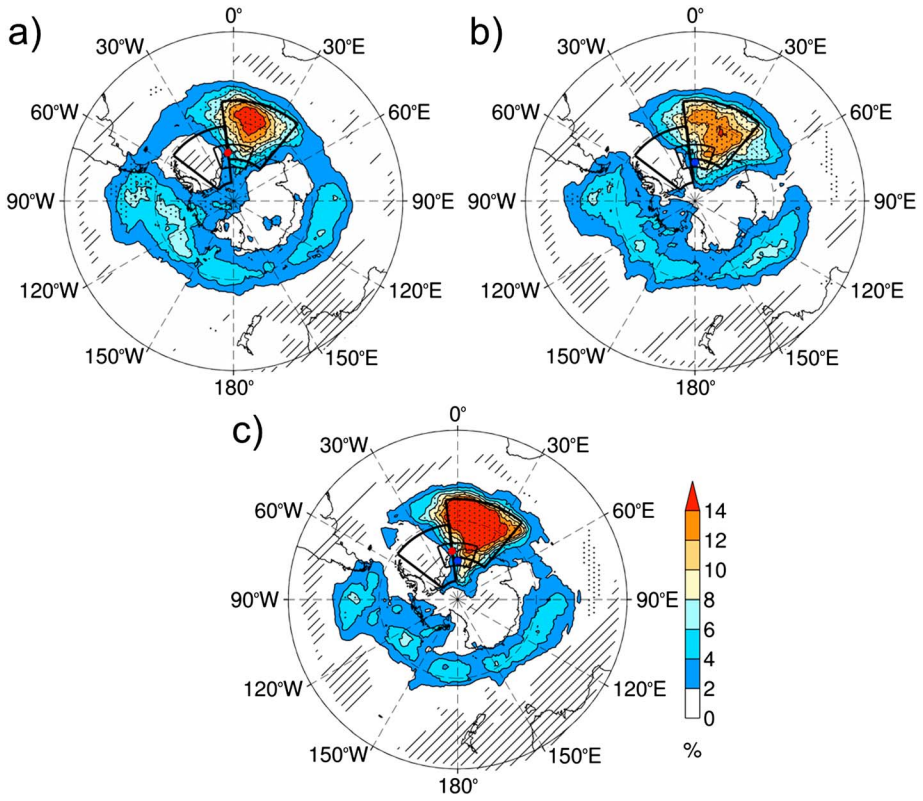

Figure 8. Analogous to Figure 5 but shown here are composites of the atmospheric blocking frequency in %. Significantly negative (positive) composites at the 5% significance level are marked with dots (diagonal lines). The domain shown in Figure 1, Boxes 1 and 2 are outlined in black (see section 3.4).

In summary, a cyclone in Box 1 is the main ingredient for high precipitation in DML, both at Halvfarryggen and at Kohnen. Although a block in Box 2 is not a requirement for high precipitation per se, the larger share of blocking occurrences during the highest-precipitation days in DML suggests an amplification of the IVT into DML when blocking in Box 2 occurs.

3.5. Precursor Signals

A high-amplitude Rossby wave train over the South Atlantic and high-amplitude moisture transport are of central relevance for the triggering of high-precipitation events in DML, and it is interesting to analyze the upstream dynamics that resulted in the formation of these favorable flow conditions.

Figure 9 shows the evolution of the upper level PV patterns for the 4 days preceding cooccurring high-precipitation events at Halvfarryggen and Kohnen. Only a weak upstream wave precursor signal is present 4 days prior to the cooccurring high-precipitation events in the form of a ridge centered at 110°W and a trough at 60°W (Figure 9a). During the next days, downstream development results in the amplified wave

Table 3. ERA-Interim High-Precipitation Days at Halvfarryggen and Kohnen Grid Points and Cooccurring Cyclones and Blocking in Boxes 1 and 2[a]

	Halvfarryggen		Kohnen		Halvfarryggen and Kohnen[b]	
	Box 1	Box 2	Box 1	Box 2	Box 1	Box 2
Cyclones	0.82	0.15	0.66	0.27	0.79	0.10
Blocking	0	0.23	0.01	0.30	0	0.37

[a]Given are fractions of 6-hourly time steps of all high-precipitation days at Halvfarryggen and Kohnen in 1979–2009 during which ≥25% of the grid cells of Boxes 1 and 2 were located within cyclones (blocks).
[b]Cooccurring high-precipitation days at Halvfarryggen and Kohnen.

Table 4. ERA-Interim High-Precipitation Days at Halvfarryggen and Kohnen Grid Points and Cooccurring Configurations[a] of Cyclones in Box 1 and Blocking in Box 2[b]

		Halvfarryggen	Kohnen	Halvfarryggen and Kohnen[c]
Box 1	Box 2			
Cyclone	blocking	0.18	0.19	0.29
Cyclone	no blocking	0.64	0.47	0.50
No cyclone	blocking	0.06	0.11	0.08
No cyclone	no blocking	0.12	0.23	0.13

[a]The configurations are described in section 3.4 and are indicated in the table.
[b]Given are fractions of 6-hourly time steps of all high-precipitation days at Halvfarryggen (Kohnen) in 1979–2009 during which ≥25% of the grid cells of Box 1 were located within cyclones and ≥25% of the grid cells of Box 2 were located within blocking; fractions for other combinations are additionally given, adding up to 1.
[c]Cooccurring high-precipitation days at Halvfarryggen and Kohnen.

pattern over the South Atlantic (Figures 9b–9e). At the same time the wave amplifies in the meridional direction (e.g., the trough at 60°W to 30°W). In parallel to the downstream development there is a hint of a statistically significant upper level PV ridge starting to form at 10°W at day 4 (Figure 9a).

Figures 10 and 11 show the evolution of surface cyclone and blocking frequencies for the 4 days preceding cooccurring high-precipitation events. A statistically significantly increased surface cyclone frequency is present over the Weddell Sea at 60°W 4 days before the high-precipitation event (Figure 10a). The pattern of statistically significantly increased surface cyclone frequency increases in amplitude and becomes spatially more extended while shifting eastward during the next days (Figures 10b–10e). Cyclone frequency increases substantially 1 day prior to the events.

The lagged composites for anomalous blocking frequency indicate already 4 days before the event an area over the South Atlantic with statistically significant anomalously high blocking frequencies (Figure 11a). Over the subsequent days the area of anomalously high blocking frequency extends, and anomalies increase while shifting slowly eastward (Figures 11b–11e).

A thorough assessment of the origin of moisture ultimately leading to high precipitation in DML can only be made by means of a Lagrangian moisture source diagnostic [e.g., *Wang et al*., 2013; *Sinclair et al*., 2013], which is beyond the scope of this study. Instead, Figure 12 gives a Eulerian perspective, showing IVT composites for the 4 days preceding the cooccurring high-precipitation events at Halvfarryggen and Kohnen. The IVT composites in Figure 12a indicate already 4 days before the high-precipitation event in DML a pattern of statistically significant anomalously high IVT over southern South America and the South Atlantic. Over the subsequent days this pattern of statistically significant IVT becomes spatially more extended while it shifts eastward (Figures 12b–12e). Furthermore, the IVT to the north of DML adopts a more and more northerly direction, which ultimately results in a pronounced poleward IVT over DML during the high-precipitation event. The moisture flux precursor signals (Figure 12) are in accordance with the temporally lagged patterns of the upper level flow, surface cyclones, and blocking (Figures 9–11).

Table 5. Absolute Frequencies of the Top 10 (Top 50) ERA-Interim Precipitation Days at Halvfarryggen and Kohnen Grid Points Associated With Prevailing Configurations[a] of Cyclones in Box 1 and Blocking in Box 2[b]

		Halvfarryggen		Kohnen	
		Top 10	Top 50	Top 10	Top 50
Box 1	Box 2				
Cyclone	blocking	5	12	1	13
Cyclone	no blocking	4	25	2	16
No cyclone	blocking	1	5	4	11
No cyclone	no blocking	0	3	1	5
Unclassified days		0	5	2	5

[a]The configurations are described in section 3.4 and are indicated in the table; the criterion for prevailing configuration we have chosen here is that a configuration (compiled for each day) lasted at least three 6-hourly time steps; high-precipitation days which could not be classified according to this criterion are listed as unclassified.
[b]The criterion we have chosen is that ≥25% of the grid cells of Box 1 (Box 2) were located within cyclones (blocks).

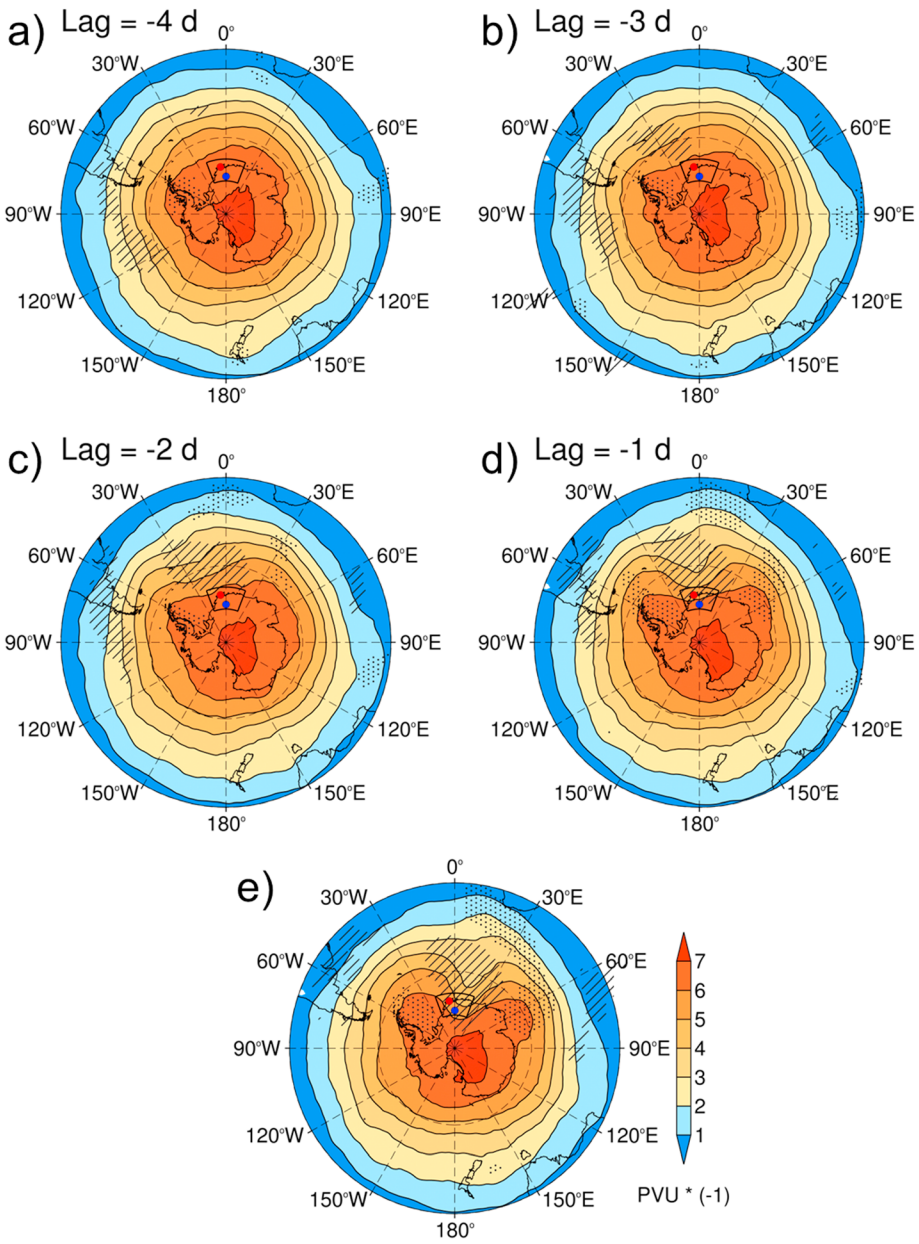

Figure 9. Analogous to Figure 6 but shown are upper level potential vorticity composites in PVU (multiplied by −1) for (e) cooccurring high-precipitation events at Halvfarryggen and Kohnen and for (a-d) the preceding 4 days. Figure 9e is the same as Figure 6c.

The lagged composites for high-precipitation events at Halvfarryggen and Kohnen alone (not shown) are similar to the composites in Figure 12 with the exception that the statistically significant areas are slightly different in spatial extent and amplitude.

Interestingly, IVT values are anomalously high and statistically significant over DML already 2 days prior to the high-precipitation events (Figure 12). At Halvfarryggen, the day before a high-precipitation event corresponds to a high-IVT day in 13% of the cases; day 2 before a high-precipitation event corresponds to a high-IVT day in 8% of the cases. The percentages are slightly higher for Kohnen with 19% and 10%. Precipitation over DML was also statistically significantly increased 2 days prior to the high-precipitation events (not shown). One explanation for this could be the longevity of the weather systems triggering the precipitation. The same cyclone can lead to precipitation over several days.

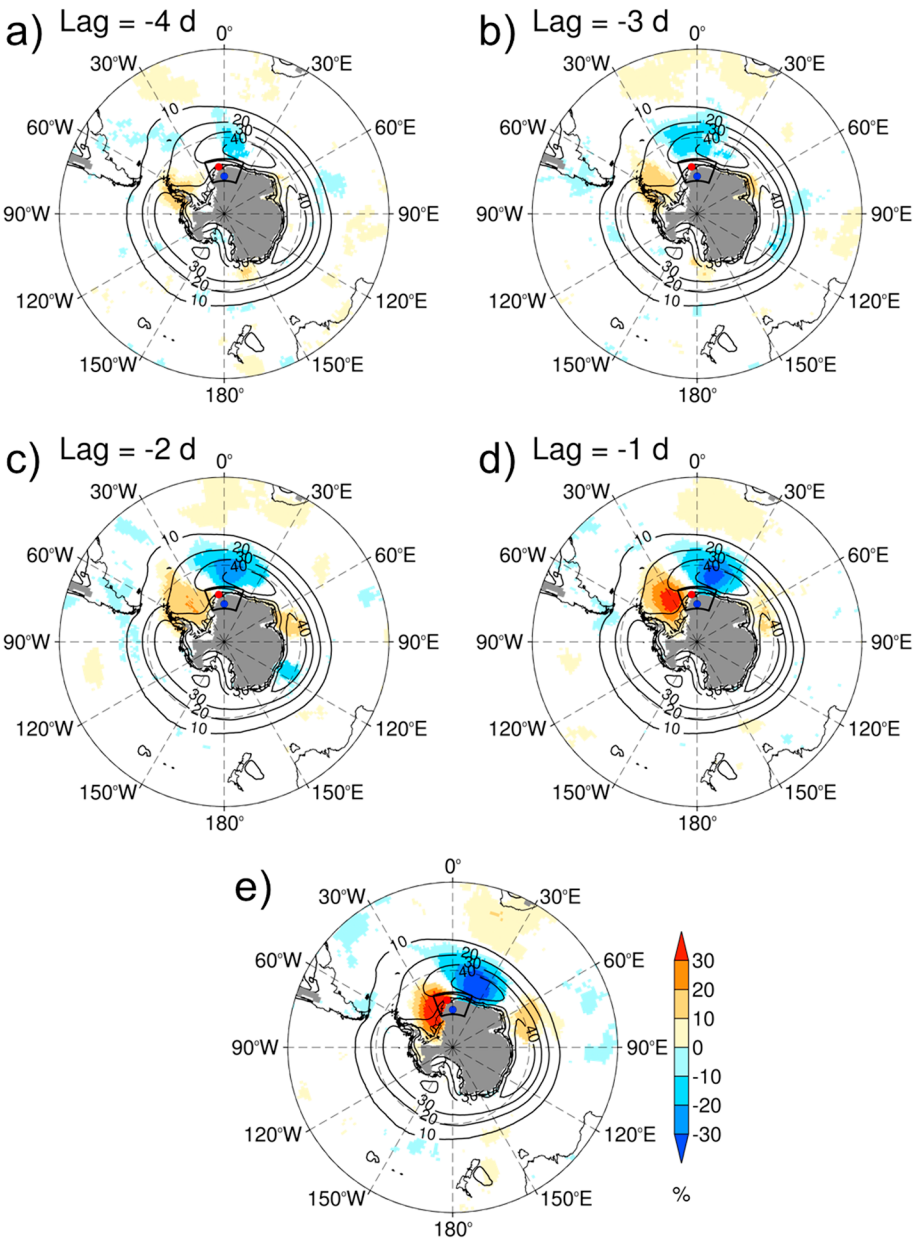

Figure 10. (e) Composites of the anomalous surface cyclone frequency in % (color shade) for cooccurring high-precipitation events at Halvfarryggen and Kohnen. Anomalies were calculated by subtracting the local climatological mean surface cyclone frequency in 1979–2009 (contours). (a-d) Evolution of the anomalous surface cyclone frequency patterns in the preceding 4 days. Only statistically significant composite averages at the 5% significance level are plotted.

4. Discussion and Main Conclusions

Based on the ERA-Interim data set for 1979–2009, we have investigated the link between the large-scale atmospheric circulation and high-precipitation events at Halvfarryggen located in the relatively wet, low-altitude coastal region of DML as well as at Kohnen Station situated in DML's dry, high-altitude interior. To describe the large-scale and synoptic atmospheric environments, we have focused on moisture transport, upper level PV, surface cyclone frequency, and atmospheric blocking frequency.

ERA-Interim precipitation data over DML have first been systematically compared with other model and observation data sets, namely with the high-resolution AMPS precipitation data and measured snow surface height changes. The main results of this comparison can be summarized as follows: while ERA-Interim and AMPS precipitation data are strongly correlated, no good correlation is found between the model-based precipitation

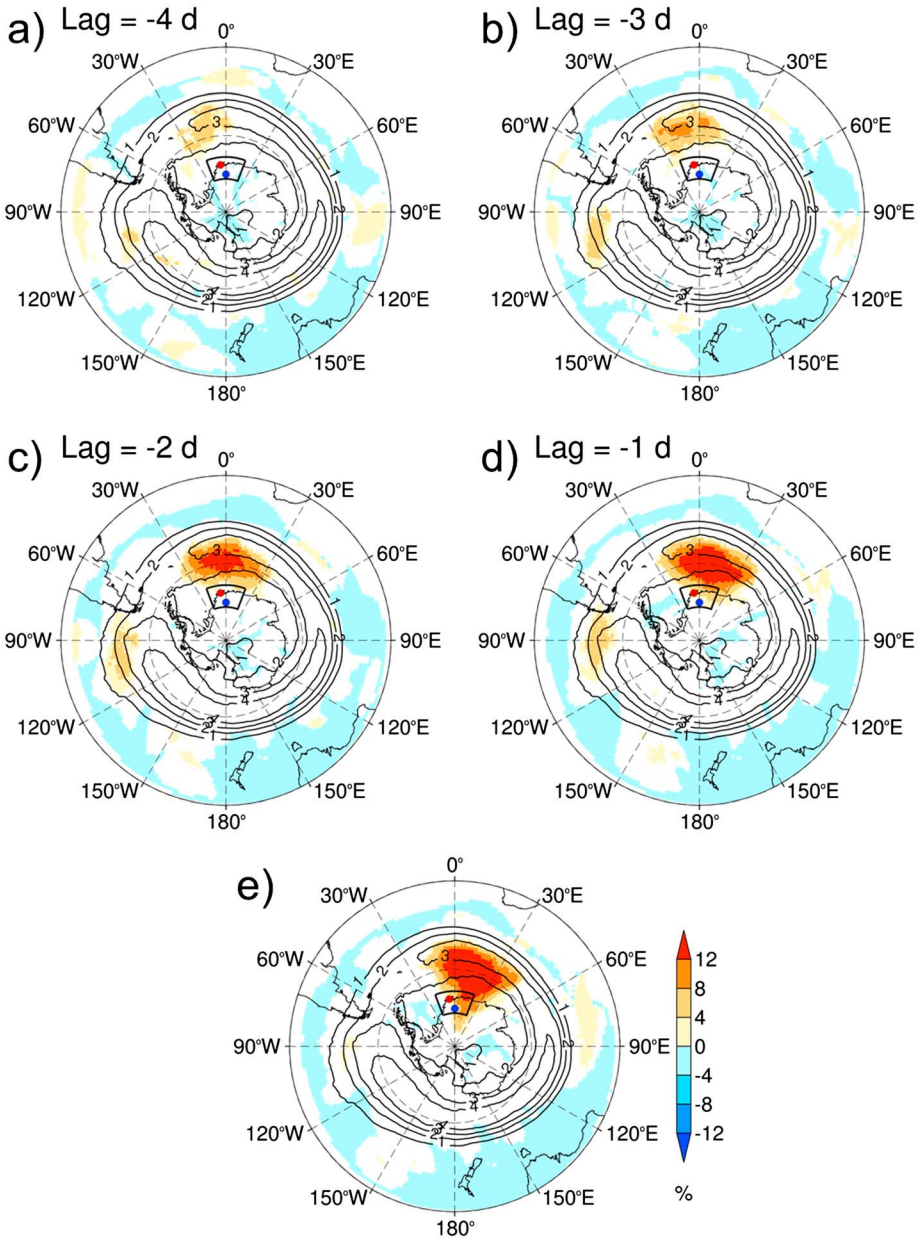

Figure 11. Analogous to Figure 10 but shown are lagged composites of the anomalous blocking frequency in %.

data sets and the measured positive snow height changes, in particular not at Kohnen. Considering high-precipitation days and high snow accumulation days at Halvfarryggen and Kohnen only, we come to the following conclusions: while high-precipitation days in the AMPS data set are generally captured by ERA-Interim, high-precipitation days in ERA-Interim do only correspond to high snow accumulation days in the AWS data in 16% (9%) of the cases at Halvfarryggen (Kohnen). These percentages are lower than those found by *Cohen and Dean* [2013] in their comparison of ERA-Interim precipitation with snow accumulation measurements from AWSs located on the Ross Ice Shelf, Antarctica. Possible reasons for that could be the different definition for precipitation and accumulation events they used, the less complex terrain of the Ross Ice Shelf which is better represented in the reanalysis compared to, e.g., Halvfarryggen, and different wind conditions on the Ross Ice Shelf influencing the snow redistribution at the AWSs.

One factor explaining at least part of the difference between model precipitation and AWS accumulation is that numerical weather prediction models tend to overestimate the number of small precipitation events

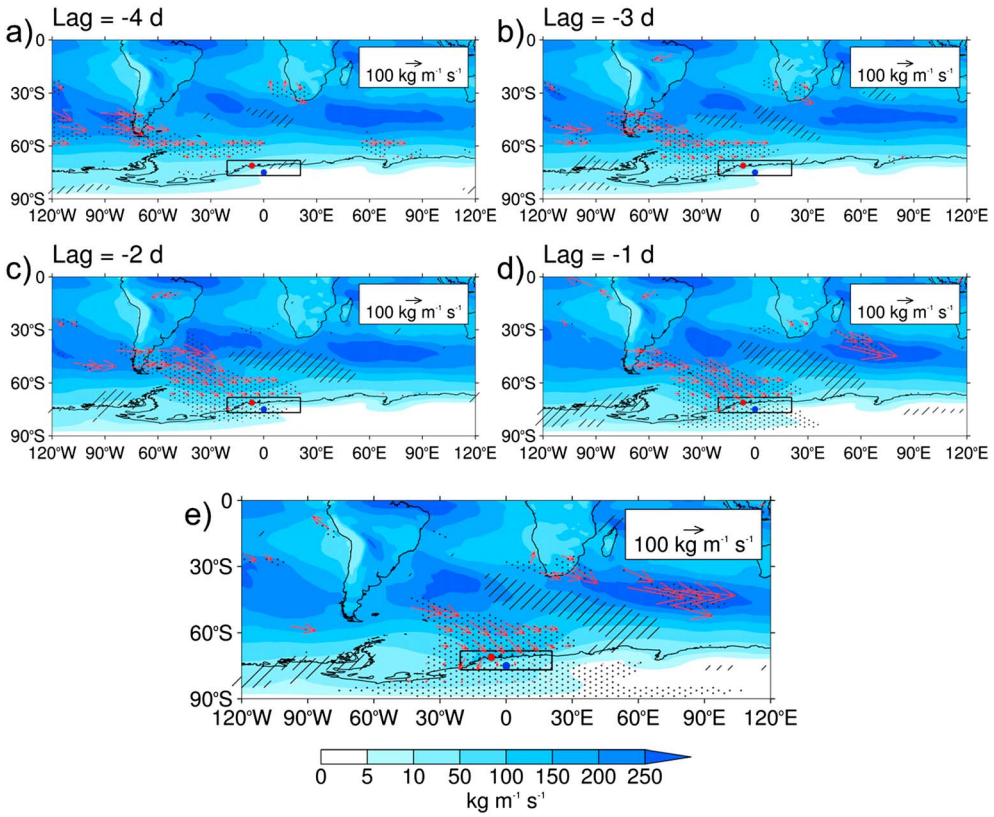

Figure 12. Analogous to Figure 5 but shown are vertically integrated water vapor transport composites (magnitude in kg m^{-1} s^{-1} and direction) for (e) cooccurring high-precipitation events at Halvfarryggen and Kohnen as well as for (a–d) the preceding 4 days. Figure 12e is the same as Figure 5c. Note the nonlinear color scale.

and underestimate the number of large events [*Reijmer et al.*, 2002]. The comparison between reanalysis products and AWS measurements is in general limited by a number of factors. There are, on the one hand, limitations of the reanalysis data due to the relatively coarse model grid resolution. One important consequence of this is that the orography is in general not realistically represented in the reanalysis, which has ramifications for the representation of, e.g., orographic precipitation in the model. On the other hand, snow accumulation changes must not necessarily be associated with precipitation but can also be due to wind-driven accumulation or ablation. In addition, the observations are partly associated with large measurement uncertainties, e.g., due to the occasional occurrence of rime on the instrument height sensor [*Reijmer and Oerlemans*, 2002]. Rime collection, however, is usually easy to detect in the AWS accumulation record.

Our results indicate that the ERA-Interim and AMPS precipitation data are more reliable over peripheral areas of DML than in the interior, given the overall better agreement between model-based precipitation and the observations at Halvfarryggen; or, vice versa, AWS data in high accumulation areas such as Halvfarryggen capture a larger share of the variability of daily precipitation values than in low accumulation areas on the Antarctic plateau. In both cases, however, the correlation between AWS-H data and ERA-I-P is low. *Palerme et al.* [2014] correspondingly showed that the agreement between ERA-Interim precipitation data and independent satellite observations of precipitation is better over peripheral areas of the Antarctic continent than over the interior. *Palerme et al.* [2014] hypothesized that the ERA-Interim data set is more reliable over peripheral areas of Antarctica, because assimilated observations, such as radiosonde humidity profiles, are more numerous there. In general, it is recommended that both model-based data of Antarctic precipitation and measured surface height changes from AWSs should be treated with caution [*Bromwich et al.*, 2011; *Schlosser et al.*, 2008] and serve different purposes (meteorological precipitation versus local surface mass balance estimates).

It is important to note that this study has assessed how well ERA-Interim precipitation is represented at Halvfarryggen and Kohnen on daily time scales. However, it has not given insight into how well ERA-Interim

represents precipitation on subdaily and longer (e.g., monthly) time scales. Furthermore, in our comparison between model precipitation and AWS accumulation we have not assessed how sensitive our results are on the possibly different timing of precipitation in the model-based data sets and in the AWS data sets.

Earlier studies suggested using the meridional atmospheric moisture flux from lower latitudes toward the Antarctic continent as a "proxy" for precipitation over Antarctica, owing to the remote location and related sparse data coverage as well as to overcome shortcomings associated with measuring snowfall and snow redistribution directly [e.g., *Tsukernik and Lynch*, 2013]. Our results confirm this finding. Indeed, we regard the large-scale IVT as one of the most relevant factors in creating high precipitation in DML's interior. Using the ERA-Interim data set, this study has shown that the high-IVT days (concerning the IVT magnitude) at Kohnen comprise 80% of the high-precipitation days at Kohnen. This study has further shown that it is important to take into account both the magnitude and the direction of the moisture fluxes. For example, high moisture fluxes over Halvfarryggen with an easterly direction do not result in high precipitation in most cases, which is due to the interaction of the moisture flux with the local orography.

The origin of air masses bringing moisture to coastal and high-plateau DML also constrains the origin of sea salt, marine biological and mineral dust aerosol tracers that are wet deposited with the events. Given that the typical lifetime of aerosol in the free troposphere is also on the order of days, this vapor transport scheme points also to an origin and efficient transport of marine tracers from the western Weddell Sea region. Moreover, our analysis allows cotransport of mineral dust aerosol from the southern tip of South America together with precipitation events. However, our analysis does not exclude that mineral dust aerosol is also transported at higher altitudes decoupled from moisture transport and is dry deposited in DML.

Our climatological investigation of the link between high precipitation in DML and the large-scale atmospheric conditions confirms and extends the findings from earlier studies, which were mainly based on case studies [e.g., *Noone et al*., 1999; *Reijmer and van den Broeke*, 2001; *Schlosser et al*., 2010a, 2010b]. We have shown that high-precipitation events at both Halvfarryggen and Kohnen were typically associated with high-amplitude waves in the upper level flow, corresponding to a PV trough located approximately at 35°W, a PV ridge at 10°E, and a PV trough at 60°E. The upper level ridge corresponds to a blocking anticyclone; for cooccurring high-precipitation days at Halvfarryggen and Kohnen, blocking occurred over the South Atlantic in more than 35% of the cases. The upper level trough-ridge-trough pattern results in a strong northerly to northwesterly flow driving the moisture transport toward Antarctica. This distinctive large-scale atmospheric flow pattern associated with high precipitation in DML is preceded by the downstream development of a Rossby wave train from the eastern Pacific sector of the Southern Ocean as early as 4 days before the precipitation event. Among others, the prevalence of the connection of this synoptic pattern with precipitation both in coastal and high-plateau DML provides significant forecasting skill for the weather conditions at DML. Furtheron, the eastward propagation of the trough located upstream of the precipitation areas results in quasi-geostrophic lifting and a destabilization of the atmosphere in the precipitation area [e.g., *Hoskins et al*., 1985], both factors would contribute to enhanced precipitation. At the surface, the wave pattern was accompanied by cyclones over the Weddell Sea resulting in a pronounced poleward moisture transport over DML; for cooccurring high-precipitation days at Halvfarryggen and Kohnen, cyclones were present over the Weddell Sea in approximately 80% of the cases.

This study has further shown that for both Halvfarryggen and Kohnen similar synoptic patterns were conducive to high precipitation. With the difference that for high precipitation at Halvfarryggen the occurrence of surface cyclones over the Weddell Sea was more important than it was for high precipitation at Kohnen. On the other hand, for high precipitation at Kohnen the presence of blocking anticyclones over the South Atlantic was more important than it was for high precipitation at Halvfarryggen. The latter finding is in accordance with *Schlosser et al*. [2010a], who emphasized the importance of atmospheric blocking related to high precipitation at Kohnen Station.

Acknowledgments

We thank three anonymous reviewers for comments that improved the quality of the manuscript. We acknowledge MeteoSwiss and ECMWF for giving access to ERA-Interim data. We give thanks to Michael Sprenger and Stephan Pfahl for making the ERA-Interim cyclone and atmospheric blocking data available. AMPS Polar WRF data are available from http://polarmet.osu.edu/AMPS/ (last access: November 2013). The IMAU AWSs were funded by the Netherlands Polar Program (NPP) and the Netherlands Organization of Scientific Research, Earth and Life Sciences section (NWO/ALW). We thank Paraskevi Giannakaki and Clément Chevalier for their assistance concerning some technical issues. Many thanks to Elisabeth Schlosser, Gerit Birnbaum, and Gert König-Langlo for valuable information and comments.

References

Altenhoff, A. M., O. Martius, M. Croci-Maspoli, C. Schwierz, and H. C. Davies (2008), Linkage of atmospheric blocks and synoptic-scale Rossby waves: A climatological analysis, *Tellus A*, *60*, 1053–1063.

Amante, C., and B. W. Eakins (2009), ETOPO1 1 arc-minute global relief model: Procedures, data sources and analysis, in *Technical Memorandum*, vol. 24, 19 pp., NOAA, Boulder, Colo.

Andersson, E., et al. (2005), Assimilation and modeling of the atmospheric hydrological cycle in the ECMWF forecasting system, *Bull. Am. Meteorol. Soc.*, *86*, 387–402.

Birnbaum, G., R. Brauner, and H. Ries (2006), Synoptic situations causing high-precipitation rates on the Antarctic plateau: Observations from Kohnen Station, DML, *Antarct. Sci.*, *18*, 279–288.
Boening, C., M. Lebsock, F. Landerer, and G. Stephens (2012), Snowfall-driven mass change on the East Antarctic ice sheet, *Geophys. Res. Lett.*, *39*, L21501, doi:10.1029/2012GL053316.
Bromwich, D. H. (1988), Snowfall in high southern latitudes, *Rev. Geophys.*, *26*, 149–168, doi:10.1029/RG026i001p00149.
Bromwich, D. H., J. P. Nicolas, and A. J. Monaghan (2011), An assessment of precipitation changes over Antarctica and the Southern Ocean since 1989 in contemporary global reanalyses, *J. Clim.*, *24*, 4189–4209.
Cohen, L., and S. Dean (2013), Snow on the Ross Ice Shelf: Comparison of reanalyses and observations from automatic weather stations, *Cryosphere*, *7*, 1399–1410.
Dee, D. P., et al. (2011), The ERA-Interim reanalysis: Configuration and performance of the data assimilation system, *Q. J. R. Meteorol. Soc.*, *137*, 553–597.
Doswell, C. A., H. E. Brooks, and R. A. Maddox (1996), Flash flood forecasting: An ingredients-based methodology, *Weather Forecasting*, *11*, 560–581.
Doswell, C. A., C. Ramis, R. Romero, and S. Alonso (1998), A diagnostic study of three heavy precipitation episodes in the Western Mediterranean region, *Weather Forecasting*, *13*, 102–124.
Enomoto, H., H. Motoyama, T. Shiraiwa, T. Saito, T. Kameda, T. Furukawa, S. Takahashi, Y. Kodama, and O. Watanabe (1998), Winter warming over Dome Fuji, East Antarctica and semiannual oscillation in the atmospheric circulation, *J. Geophys. Res.*, *103*, 23,103–23,111, doi:10.1029/98JD02001.
EPICA Community Members (2006), One-to-one coupling of glacial climate variability in Greenland and Antarctica, *Nature*, *444*, 195–198.
Gorodetskaya, I. V., N. P. M. van Lipzig, M. R. van den Broeke, A. Mangold, W. Boot, and C. H. Reijmer (2013), Meteorological regimes and accumulation patterns at Utsteinen, Dronning Maud Land, East Antarctica: Analysis of two contrasting years, *J. Geophys. Res. Atmos.*, *118*, 1700–1715.
Gregory, J. M., and P. Huybrechts (2006), Ice-sheet contributions to future sea-level change, *Philos. Trans. R. Soc. A*, *364*, 1709–1731.
Hirasawa, N., H. Nakamura, and T. Yamanouchi (2000), Abrupt changes in meteorological conditions observed at an inland Antarctic station in association with a wintertime blocking, *Geophys. Res. Lett.*, *27*, 1911–1914, doi:10.1029/1999GL011039.
Hirasawa, N., H. Nakamura, H. Motoyama, M. Hayashi, and T. Yamanouchi (2013), The role of synoptic-scale features and advection in prolonged warming and generation of different forms of precipitation at Dome Fuji Station, Antarctica, following a prominent blocking event, *J. Geophys. Res. Atmos.*, *118*, 6916–6928, doi:10.1002/jgrd.50532.
Hoskins, B. J., M. E. McIntyre, and A. W. Robertson (1985), On the use and significance of isentropic potential vorticity maps, *Q. J. R. Meteorol. Soc.*, *111*, 877–946.
King, J. C., and J. Turner (1997), *Antarctic Meteorology and Climatology*, Cambridge Univ. Press, Cambridge, U. K.
Lavers, D. A., G. Villarini, R. P. Allan, E. F. Wood, and A. J. Wade (2012), The detection of atmospheric rivers in atmospheric reanalyses and their links to British winter floods and the large-scale climatic circulation, *J. Geophys. Res.*, *117*, D20106, doi:10.1029/2012JD018027.
Lenaerts, J. T. M., M. R. van den Broeke, W. J. van de Berg, E. van Meijgaard, and P. Kuipers Munneke (2012), A new, high-resolution surface mass balance map of Antarctica (1979–2010) based on regional atmospheric climate modeling, *Geophys. Res. Lett.*, *39*, L04501, doi:10.1029/2011GL050713.
Lenaerts, J. T. M., E. van Meijgaard, M. R. van den Broeke, S. R. M. Ligtenberg, M. Horwath, and E. Isaksson (2013), Recent snowfall anomalies in Dronning Maud Land, East Antarctica, in a historical and future climate perspective, *Geophys. Res. Lett.*, *40*, 2684–2688, doi:10.1002/grl.50559.
Marshall, G. J. (2003), Trends in the Southern Annular Mode from observations and reanalyses, *J. Clim.*, *16*, 4134–4143.
Nicolas, J. P., and D. H. Bromwich (2011), Precipitation changes in high southern latitudes from global reanalyses: A cautionary tale, *Surv. Geophys.*, *32*, 475–494.
Noone, D., J. Turner, and R. Mulvaney (1999), Atmospheric signals and characteristics of accumulation in Dronning Maud Land, Antarctica, *J. Geophys. Res.*, *104*, 19,191–19,211, doi:10.1029/1999JD900376.
Palerme, C., J. E. Kay, C. Genthon, T. L'Ecuyer, N. B. Wood, and C. Claud (2014), How much snow falls on the Antarctic ice sheet?, *Cryosphere Discuss.*, *8*, 1279–1304.
Pfahl, S., and H. Wernli (2012), Quantifying the relevance of cyclones for precipitation extremes, *J. Clim.*, *25*, 6770–6780.
Pfahl, S., E. Madonna, M. Boettcher, H. Joos, and H. Wernli (2014), Warm conveyor belts in the ERA-Interim dataset (1979–2010). Part II: Moisture origin and relevance for precipitation, *J. Clim.*, *27*, 27–40.
Powers, J. G., A. J. Monaghan, A. M. Cayette, D. H. Bromwich, Y. Kuo, and K. W. Manning (2003), Real-time mesoscale modeling over Antarctica: The Antarctic Mesoscale Prediction System, *Bull. Am. Meteorol. Soc.*, *84*, 1522–1545.
Powers, J., K. W. Manning, D. H. Bromwich, J. J. Cassano, and A. M. Cayette (2012), A decade of Antarctic science support through AMPS, *Bull. Am. Meteorol. Soc.*, *93*, 1699–1712.
Reijmer, C. H., and J. Oerlemans (2002), Temporal and spatial variability of the surface energy balance in Dronning Maud Land, East Antarctica, *J. Geophys. Res.*, *107*(D24), 4759, doi:10.1029/2000JD000110.
Reijmer, C. H., and M. R. van den Broeke (2001), Moisture source of precipitation in Western Dronning Maud Land, Antarctica, *Antarct. Sci.*, *13*, 210–220.
Reijmer, C. H., and M. R. van den Broeke (2003), Temporal and spatial variability of the surface mass balance in Dronning Maud Land, Antarctica, *J. Glaciol.*, *49*, 512–520.
Reijmer, C. H., M. R. van den Broeke, and M. P. Scheele (2002), Air parcel trajectories and snowfall related to five deep drilling locations in Antarctica based on the ERA-15 dataset, *J. Clim.*, *15*, 1957–1968.
Rotschky, G., P. Holmlund, E. Isaksson, R. Mulvaney, H. Oerter, M. R. van den Broeke, and J.-G. Winther (2007), A new surface accumulation map for western Dronning Maud Land, Antarctica, from interpolation of point measurements, *J. Glaciol.*, *53*, 385–398.
Schlosser, E., M. G. Duda, J. G. Powers, and K. W. Manning (2008), Precipitation regime of Dronning Maud Land, Antarctica, derived from Antarctic Mesoscale Prediction System (AMPS) archive data, *J. Geophys. Res.*, *113*, D24108, doi:10.1029/2008JD009968.
Schlosser, E., K. W. Manning, J. G. Powers, M. G. Duda, G. Birnbaum, and K. Fujita (2010a), Characteristics of high-precipitation events in Dronning Maud Land, Antarctica, *J. Geophys. Res.*, *115*, D14107, doi:10.1029/2009JD013410.
Schlosser, E., J. G. Powers, M. G. Duda, K. W. Manning, C. H. Reijmer, and M. R. van den Broeke (2010b), An extreme precipitation event in Dronning Maud Land, Antarctica: A case study with the Antarctic Mesoscale Prediction System, *Polar Res.*, *29*, 330–344.
Schlosser, E., J. G. Powers, M. G. Duda, and K. W. Manning (2011), Interaction between Antarctic sea ice and synoptic activity in the circumpolar trough: Implications for ice-core interpretation, *Ann. Glaciol.*, *52*, 9–17.
Schwierz, C., M. Croci-Maspoli, and H. C. Davies (2004), Perspicacious indicators of atmospheric blocking, *Geophys. Res. Lett.*, *31*, L06125, doi:10.1029/2003GL019341.

Shutts, G. J. (1983), The propagation of eddies in diffluent jetstreams: Eddy vorticity forcing of 'blocking' flow fields, *Q. J. R. Meteorol. Soc.*, *109*, 737–761.

Sinclair, K. E., N. A. N. Bertler, W. J. Trompetter, and W. T. Baisden (2013), Seasonality of airmass pathways to coastal Antarctica: Ramifications for interpreting high-resolution ice core records, *J. Clim.*, *26*, 2065–2076.

Skamarock, W. C., J. B. Klemp, J. Dudhia, D. O. Gill, D. M. Barker, M. G. Duda, X.-Y. Huang, W. Wang, and J. G. Powers (2008), A description of the advanced research WRF version 3, *Tech. Note 475+STR*, 113 pp., Natl. Cent. for Atmos. Res., Boulder, Colo.

Sprenger, M., O. Martius, and J. Arnold (2013), Cold surge episodes over southeastern Brazil—A potential vorticity perspective, *Int. J. Climatol.*, *33*, 2758–2767.

Tsukernik, M., and A. H. Lynch (2013), Atmospheric meridional moisture flux over the Southern Ocean: A story of the Amundsen Sea, *J. Clim.*, *26*, 8055–8064.

Uppala, S., D. Dee, S. Kobayashi, P. Berrisford, and A. Simmons (2008), Towards a climate data assimilation system: Status update of ERA-Interim, *ECMWF Newsl.*, *115*, 12–18.

Wang, Y., H. Sodemann, S. Hou, V. Masson-Delmotte, J. Jouzel, and H. Pang (2013), Snow accumulation and its moisture origin over Dome Argus, Antarctica, *Clim. Dyn.*, *40*, 731–742.

Wernli, H., and C. Schwierz (2006), Surface cyclones in the ERA-40 dataset (1958–2001). Part I: Novel identification method and global climatology, *J. Atmos. Sci.*, *63*, 2486–2507.

Ye, H., E. J. Fetzer, D. H. Bromwich, E. F. Fishbein, E. T. Olsen, S. L. Granger, S.-Y. Lee, L. Chen, and B. H. Lambrigtsen (2007), Atmospheric total precipitable water from AIRS and ECMWF during Antarctic summer, *Geophys. Res. Lett.*, *34*, L19701, doi:10.1029/2006GL028547.